energies

MDPI

Article

Multi-Time-Scale Power and Energy Balance Optimization Method for Power Systems Considering Hydrogen Energy Storage Failures Under Dynamic Carbon Quota Allocation

Hanyue Liu [1,2], Hangyu Niu [1,2], Qian Ma [3], Zening Li [1,2], Wenzhuo Zhu [1,2], Pengshu Wang [1,2], Fei Zhao [1,2] and Ke Wang [4,*]

[1] College of Electrical and Power Engineering, Taiyuan University of Technology, Taiyuan 030024, China; 2024510357@link.tyut.edu.cn (H.L.); 2025520527@link.tyut.edu.cn (H.N.); lizening@tyut.edu.cn (Z.L.); 2025520588@link.tyut.edu.cn (W.Z.); 2025520551@link.tyut.edu.cn (P.W.); 2025510294@link.tyut.edu.cn (F.Z.)
[2] Shanxi Energy Internet Engineering Research Center, Taiyuan 030024, China
[3] China Southern Power Grid Company Limited, Guangzhou 510663, China; maqian@csg.cn
[4] State Grid Tianjin Electric Power Research Institute, Tianjin 300384, China
* Correspondence: wang_ke@aliyun.com

Abstract

High renewable energy penetration significantly increases source-side uncertainty and makes power and energy balancing more difficult under carbon emission constraints. To improve the multi-time-scale power and energy balance of highly uncertain power systems, this paper proposes a low-carbon coordinated optimization method considering wind–photovoltaic output uncertainty, hydrogen energy storage availability uncertainty, and carbon quota constraints. Wind and photovoltaic uncertainty is described by joint scenarios, while the available capacities of electrolyzers and hydrogen fuel cells are characterized using Markov-chain-based capacity coefficients. On this basis, a multi-time-scale power and energy balance optimization framework is established by combining medium- and long-term stochastic energy task decomposition, day-ahead two-stage stochastic optimization, and intra-day model predictive control rolling correction. The medium- and long-term layer coordinates energy tasks and carbon budgets, the day-ahead layer forms a baseline power and energy balance plan, and the intra-day layer corrects real-time power deviations. In addition, a dynamic carbon quota mechanism related to load level, renewable energy penetration, and hydrogen energy storage system availability is introduced to reflect the impact of operating conditions on low-carbon scheduling. Case-study results show that the proposed method can maintain power and energy balance under renewable fluctuations and hydrogen energy storage availability variations. Compared with a static carbon quota scheme, the dynamic carbon quota mechanism reduces total operating cost by 8.94% and carbon emissions by 8.77%. The intra-day rolling correction reduces the RMSE of residual power deviations to 9.39 kW, indicating that the proposed optimization method can improve multi-time-scale balancing robustness and low-carbon operation capability of highly uncertain power systems.

Keywords: power and energy balance; dynamic carbon quota; hydrogen energy storage failures; multi-time-scale scheduling

Check for updates

Academic Editors: Andrea De Pascale and Alan Brent

Received: 8 July 2026
Revised: 10 September 2026
Accepted: 28 September 2026
Published: 8 October 2026

Copyright: © 2026 by the authors. Licensee MDPI, Basel, Switzerland. This article is an open access article distributed under the terms and conditions of the Creative Commons Attribution (CC BY) license.

1. Introduction

Against the background of the continuous advancement of China's "dual-carbon" strategic goals and the accelerated development of new-type power systems, the installed

capacity and generation share of renewable energy sources, represented by wind power and photovoltaic power, have continued to increase [1]. However, renewable energy output is significantly affected by meteorological conditions and is characterized by strong randomness, volatility, and intermittency, which substantially increases source-side uncertainty in power systems and further intensifies power and energy balance pressures [2,3]. With the continuous increase in renewable energy penetration, power system balancing is no longer limited to power matching within a single time period, but has gradually evolved into a multi-time-scale coordination problem of power and energy covering medium- and long-term planning, day-ahead scheduling, intra-day adjustment, and real-time operation. Under increasingly stringent carbon emission constraints, how to coordinate multiple types of flexibility resources, including generation, load, and energy storage, enhance the multi-time-scale power and energy balancing capability of the system under highly uncertain scenarios, and ensure the safe, economic, and low-carbon operation of power systems has become a critical issue that urgently needs to be addressed in the operation optimization of new-type power systems.

To address the multi-time-scale power and energy balancing problem under high uncertainty, power systems require flexible resources that can provide both short-term power regulation and cross-period energy transfer. Electrochemical energy storage can rapidly smooth renewable output fluctuations and load variations, but its limited capacity and discharge duration restrict its ability to independently support long-duration energy balancing in high-renewable-penetration systems. Hydrogen energy storage can absorb surplus renewable electricity through hydrogen production and reconvert stored hydrogen into electricity when needed, thereby providing complementary flexibility for renewable energy accommodation, long-duration storage, and multi-time-scale power and energy balancing [4,5].

Existing studies have widely investigated the role of hydrogen energy storage in enhancing system flexibility, renewable energy accommodation, and power and energy balancing capability. These studies generally show that electrolyzers, hydrogen fuel cells, hydrogen storage, energy storage, and demand response can be coordinated to improve the adaptability of power systems, integrated energy systems, and microgrids under renewable energy fluctuations [6–10]. Furthermore, Wang et al. [11] investigated a multi-time-scale optimization framework for integrated energy systems with diversified hydrogen energy utilization, where hydrogen storage, hydrogen conversion pathways, and coupled green certificate–carbon trading mechanisms were jointly considered to improve renewable energy accommodation and low-carbon operation. Song et al. [12] proposed a multi-time-scale optimization model considering long-term and short-term hydrogen storage, demand response, and multiple uncertainties, demonstrating the potential of hydrogen storage for improving renewable energy accommodation. Li et al. [13] considered multi-time-scale operations of electricity–hydrogen integrated energy systems and explored the interaction between different storage technologies. However, most of them assume that hydrogen energy devices are fully available during operation, while the impacts of equipment state uncertainty, such as failures, derated operation, and unplanned outages, are not sufficiently considered. In practical operation, changes in the available capacity of electrolyzers and fuel cells may directly weaken the power regulation capability of hydrogen energy storage and, by altering hydrogen production and storage levels, further affect subsequent power support and cross-period energy transfer. Therefore, it is necessary to incorporate hydrogen energy storage equipment state uncertainty into the analysis of multi-time-scale power and energy balance, so as to evaluate its influence on the power and energy balance capability.

Under carbon emission constraints, power and energy balancing in power systems is not only a physical supply–demand matching problem, but also a low-carbon alloca-

tion problem affected by emission allowances and carbon trading mechanisms. Existing studies have introduced carbon trading, ladder-type carbon pricing, demand response, green certificate trading, and carbon capture into low-carbon scheduling models, showing that these mechanisms can effectively reduce carbon emissions and improve operational economy [14–17]. Shi et al. [18] further considered the allocation of carbon allowances across multiple time-scales and proposed a low-carbon economic dispatch framework for integrated energy systems under uncertainty, in which carbon emission constraints were coordinated with system operation at different temporal levels. Wang et al. [19] further incorporated hydrogen utilization and carbon trading mechanisms into an integrated energy system optimization model, where a two-stage robust optimization method was developed to coordinate economic operation and emission reduction under uncertainty. Zhao et al. [20] investigated multi-time-scale carbon trading mechanisms in hydrogen-integrated energy systems and established a scheduling framework considering the interaction between hydrogen utilization and carbon-market signals. However, most existing models describe carbon constraints using fixed emission factors, static allowances, or predetermined baselines, which makes it difficult to reflect the influence of time-varying operating conditions on carbon responsibility allocation. In highly uncertain power systems, load levels, renewable energy output, and the availability of flexibility resources may vary significantly across different scheduling periods. If the carbon quotas allocated to individual scheduling periods remain static, carbon constraints may be too strict in some periods and too loose in others, thereby affecting the rationality of power and energy balancing results. Therefore, it is necessary to develop a dynamic carbon quota allocation mechanism for multi-time-scale power and energy balance analysis, so that the prescribed daily carbon budget can be dynamically redistributed among scheduling periods according to load level, renewable energy penetration, and hydrogen energy equipment availability, while keeping the total daily carbon budget unchanged.

With the integration of a high proportion of renewable energy, power and energy balancing is no longer confined to a single time-scale, but exhibits evident cross-time-scale coupling characteristics. At the medium- and long-term level, periodic energy tasks and carbon emission budgets need to be coordinated; at the day-ahead level, baseline operation schedules need to be formulated based on forecast information; and at the intra-day and real-time levels, schedule deviations need to be corrected in a rolling manner according to changes in renewable energy output, load demand, and equipment operating states [21]. To address the propagation effects of source–load forecasting errors during schedule execution, existing studies have explored multi-time-scale coordinated scheduling and model predictive control. Reference [22] established a day-ahead–intra-day multi-time-scale optimal scheduling model considering source–load uncertainty, realizing coordinated control of system resources across different time-scales. Furthermore, He et al. [23] integrated light robust optimization with model predictive control into a day-ahead–intra-day scheduling framework, where intra-day rolling optimization and feedback correction were employed to enhance the adaptability of microgrid operation under source–load prediction errors. Reference [24] proposed a real-time economic dispatch strategy for microgrids based on model predictive control, in which rolling optimization and feedback correction were employed to improve system adaptability to renewable energy and load forecasting errors. Reference [25] proposed a model-predictive-control-based real-time scheduling method for integrated energy systems with Power-to-X devices, aiming to balance the impacts of multi-source uncertainty on system operation. Fang et al. [26] further developed a multi-stage and multi-time-scale energy management framework for hydrogen-based integrated energy systems, integrating day-ahead scheduling, MPC-based intra-day rolling dispatch, and real-time adjustment to coordinate electricity–hydrogen–heat balance un-

der demand uncertainties. Reference [27] developed a convex model predictive control method for battery energy storage systems in distributed microgrids, enabling real-time optimal allocation of energy storage power. Yang et al. [28] developed a distributionally robust optimization-based scheduling framework for hydrogen-coupled integrated energy systems considering carbon trading and demand response, where uncertainty in renewable energy and load demand was addressed through robust optimization. The above studies provide effective methods for multi-time-scale coordinated operation under highly uncertain scenarios. However, existing studies mostly regard day-ahead schedules or upper-level decomposed tasks as deterministic references, with emphasis placed on the rolling correction of intra-day renewable energy output and load forecasting errors, while insufficient attention has been paid to the uncertainty of medium- and long-term power and energy decomposition plans themselves and their propagation effects on the day-ahead and intra-day execution levels. If such uncertainty is ignored, lower-level scheduling may struggle to simultaneously satisfy energy task requirements, power and energy balance, and carbon emission constraints during execution. Therefore, it is necessary to develop a closed-loop multi-time-scale rolling optimization framework that accounts for uncertainty in medium- and long-term task decomposition, thereby realizing coordinated linkage among medium- and long-term planning, day-ahead baseline scheduling, and intra-day feedback correction. The realized generation and carbon emissions can then be fed back to update subsequent upper-level tasks, maintaining consistency between short-term operation and medium- and long-term energy and emission objectives.

A comparison of the proposed method with representative existing studies is presented in Table 1.

Table 1. Comparison of the proposed method with recent representative existing studies on low-carbon power system scheduling.

Study	Multi-Time-Scale Scheduling	Uncertainty-Aware Optimization	Hydrogen Energy Storage	HES Failure/Derating	Carbon Constraint Mechanism	MPC	Cross-Time-Scale Energy–Carbon Coordination
Turk et al. (2021) [25]	×	✓	×	×	×	✓	×
Wu et al. (2022) [21]	✓	✓	×	×	×	✓	×
Huang et al. (2023) [22]	✓	✓	×	×	×	×	×
He et al. (2023) [23]	✓	✓	×	×	×	✓	×
Shi et al. (2023) [18]	✓	✓	×	×	✓	×	×
Fang et al. (2024) [26]	✓	✓	✓	×	×	✓	×
Wang et al. (2024) [11]	✓	✓	✓	×	✓	✓	×
Song et al. (2024) [12]	✓	✓	✓	×	✓	×	×
Li et al. (2024) [13]	✓	×	✓	×	×	×	×
Wang et al. (2025) [19]	×	✓	✓	×	✓	×	×
Zhao et al. (2025) [20]	✓	×	✓	×	✓	×	×
Yang et al. (2025) [24]	×	✓	✓	×	✓	×	×
Proposed method	✓	✓	✓	✓	✓	✓	✓

Based on the above analysis, this paper proposes a multi-time-scale power and energy balance optimization method for highly uncertain power systems considering hydrogen

energy storage system failures and state-coupled dynamic carbon quota allocation. The main contributions are summarized as follows:

1. A source–load–storage coordinated optimization model considering hydrogen energy storage equipment failures is established. A Markov-chain-based multi-state availability model is used to characterize the normal, derated, and outage states of electrolyzers and hydrogen fuel cells, and the corresponding available capacity coefficients are embedded into electricity–hydrogen operation constraints. The model therefore captures not only the instantaneous reduction in power regulation capability caused by equipment failures, but also their intertemporal impact on hydrogen storage and cross-period energy transfer.
2. A state-coupled dynamic carbon quota mechanism for low-carbon power and energy balance optimization under carbon emission constraints is proposed. The prescribed daily carbon budget is dynamically redistributed among scheduling periods according to load level, renewable energy penetration, and hydrogen energy storage availability while maintaining the total daily carbon budget unchanged. By coupling carbon allocation with both operating conditions and available system flexibility, the proposed mechanism improves the coordination between economic operation, power–energy balance, and carbon emission reduction.
3. A closed-loop multi-time-scale power and energy balance optimization method considering uncertainty in upper-level task decomposition is developed. Medium- and long-term stochastic task decomposition, day-ahead two-stage stochastic optimization, and intra-day MPC are coordinated through explicit generation-task and carbon budget tracking. The intra-day MPC not only corrects day-ahead power deviations but also continuously coordinates the remaining generation task and carbon budget, while realized generation and emissions are fed back to update subsequent upper-level tasks.

2. Materials and Methods

2.1. System Configuration and Balance Analysis Framework

The proposed framework focuses on the multi-time-scale power and energy balance of a grid-connected power system with high renewable energy penetration under carbon emission constraints. As shown in Figure 1, the system consists of wind turbines, photovoltaic units, thermal power units, an electrical energy storage system (ESS), electrolyzers (ELs), hydrogen fuel cells (HFCs), loads, and the external power grid. Wind and photovoltaic generation are the main renewable energy sources, while thermal units and grid interaction provide conventional power support. ESS is used for short-term power regulation, whereas the EL and HFC realize electricity–hydrogen conversion, providing additional flexibility for renewable energy accommodation and power balancing.

To clarify the carbon emission accounting scope, the system boundary is defined with reference to the goal-and-scope principle of ISO 14040 and ISO 14044 [29,30]. Since this study focuses on multi-time-scale operational scheduling rather than full life-cycle assessment, only carbon emissions occurring within the operational boundary of the modeled power system are considered. Specifically, the carbon emission accounting includes direct CO_2 emissions from thermal power generation within the system and operational emissions associated with electricity imported from the external grid. Wind power, photovoltaic generation, ESS, ELs, hydrogen storage, and HFCs are treated as zero direct-emission resources during operation. Life-cycle emissions associated with raw-material extraction, equipment manufacturing, transportation, construction, maintenance, replacement, and end-of-life treatment are outside the scope of this study. The emissions associated with electricity consumed by ESS and hydrogen conversion devices are attributed to the corre-

sponding electricity supply sources rather than being separately counted, so as to avoid double counting. Therefore, the carbon emission results reported in this study represent operational carbon emissions within the defined system boundary rather than full life-cycle greenhouse-gas emissions.

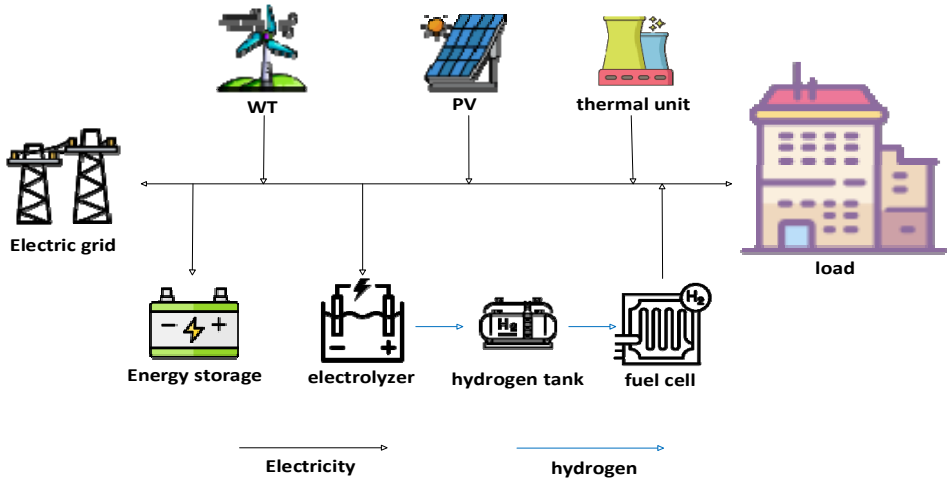


Figure 1. System configuration of the electricity–hydrogen coupled power system.

2.2. Uncertainty Modeling of Wind–Solar Power Output and Hydrogen Energy Equipment States

The power outputs of wind turbines and photovoltaic systems exhibit significant randomness and intermittency, which introduce considerable uncertainty into renewable energy generation. Since this study focuses on system-level power and energy balance optimization rather than meteorological forecasting, renewable-generation uncertainty is characterized directly at the power-output level. Specifically, annual synthetic hourly WT and PV power profiles covering 365 consecutive days described in Section 3.1 are used to construct empirical power-output distributions and generate joint renewable-power scenarios for stochastic optimization. Therefore, wind speed and solar irradiance are not explicitly modeled in the numerical case study.

2.2.1. Wind–Photovoltaic Joint Scenario Generation

Since wind power and photovoltaic output exhibit significant randomness and intermittency, this paper adopts a scenario-based method to characterize their joint uncertainty. The renewable-generation scenarios used in the stochastic optimization are constructed directly from empirical power-output distributions. Specifically, the 365-day synthetic hourly WT and PV power series covering a complete annual cycle described in Section 3.1 are used to construct empirical power-output distributions. The annual dataset incorporates seasonal variations in renewable-generation characteristics, enabling the scenario-generation process to capture both short-term stochastic fluctuations and seasonal differences in renewable energy availability.

Based on these distributions, 500 joint WT–PV power scenarios are generated through Monte Carlo sampling. The K-means clustering algorithm is then used to reduce the original scenario set to five representative scenarios for stochastic optimization, thereby reducing computational complexity while retaining the main statistical characteristics of renewable generation.

2.2.2. Markov-Chain-Based Multi-State Availability Model of Hydrogen Energy Storage Equipment

For the PEM electrolyzer considered in this study, equipment unavailability may arise from stack-level degradation and balance-of-plant abnormalities. Degradation of

key electrochemical components may increase electrochemical and ohmic losses, while hydrogen crossover and auxiliary-system abnormalities, such as water-supply, thermal-management, and pressure-control problems, may restrict the admissible operating range or lead to temporary shutdown [31,32]. In addition, variable-power operation and frequent start–stop events may affect equipment degradation and availability [32]. Since the objective of this study is system-level power and energy balance optimization rather than component-level degradation diagnosis, these physical effects are aggregated into three availability states—normal, derated, and outage—and represented by corresponding available capacity coefficients.

The normal state represents unrestricted operation within the rated capacity; the derated state represents partial loss of available production capacity caused by degradation or auxiliary-system limitations; and the outage state represents a condition in which the EL is unavailable because of severe faults or protective shutdown. Accordingly, the physical consequences of EL faults are represented in the optimization model through a time-varying available capacity coefficient rather than by explicitly modeling individual electrochemical degradation processes.

$$\mathbf{M} = \begin{bmatrix} -\lambda_{01} - \lambda_{02} & \lambda_{01} & \lambda_{02} \\ \mu_{10} & -\mu_{10} - \lambda_{12} & \lambda_{12} \\ \mu_{20} & \mu_{21} & -\mu_{20} - \mu_{21} \end{bmatrix} \tag{1}$$

Specifically, λ_{ij} denotes the transition rate from state i to state j associated with equipment degradation or failure evolution, while μ_{ij} represents the recovery transition rate from an unavailable or degraded state to a higher availability state.

By solving the steady-state algebraic equation set,

$$\begin{cases} \boldsymbol{\pi}\mathbf{M} = 0 \\ \sum\limits_{i \in S} \pi_i = 1 \end{cases} \tag{2}$$

where $\boldsymbol{\pi} = [\pi_0, \pi_1, \pi_2]$ denotes the steady-state probability of the equipment being in each state. Accordingly, the expected available capacity coefficient of the equipment in the day-ahead scheduling stage can be obtained as follows:

$$\overline{\alpha}^m = \pi_0^m \alpha_0^m + \pi_1^m \alpha_1^m + \pi_2^m \alpha_2^m \tag{3}$$

The obtained availability coefficient is further embedded into the operating constraints of ELs and HFCs, where the maximum available charging and discharging capacities are adjusted according to the stochastic equipment states. Therefore, the proposed model captures the impact of hydrogen equipment failures on system power and energy balance optimization.

Based on the above physical interpretation, State 0 represents normal operation, in which the EL can operate up to its nominal available capacity. State 1 represents derated operation, in which degradation or auxiliary-system limitations reduce the maximum admissible operating power while hydrogen production remains possible. State 2 represents complete outage, corresponding to severe faults or protective shutdown, and the available EL power is therefore set to zero. The transition from State 0 to State 1 describes progressive performance deterioration or a recoverable operating limitation; the transition from State 0 or State 1 to State 2 represents a more severe failure leading to shutdown; and the reverse transitions represent recovery following fault clearance or maintenance. The Markov

transition rates are therefore interpreted as system-level availability transition parameters rather than the degradation rates of individual electrochemical components.

$$\alpha_0^m = 1,\ \alpha_1^m = \rho^m,\ \alpha_2^m = 0 \tag{4}$$

$$\overline{\alpha}^m = \pi_0^m + \rho^m \pi_1^m \tag{5}$$

where $m \in \{EL,HFC\}$ denotes the EL or HFC; $\rho_m \in (0,1)$ is the available capacity coefficient when the equipment is in the derated state. State 2 is outage; therefore, the corresponding available capacity is 0.

The transition rates and available capacity coefficients are introduced to characterize the availability uncertainty of hydrogen energy equipment. The transition rates describe the relative tendencies among normal operation, degraded operation, and outage states, while the available capacity coefficient reflects the remaining available capacity under degraded operation. As shown in Table 2, the transition rates and available capacity coefficients of the EL and HFC are specified to represent their respective availability characteristics. Because component-level field failure and maintenance records are not available for the representative test system considered in this study, the parameters in Table 2 are not obtained through statistical fitting of a specific device dataset. Instead, representative characteristic transition and recovery times are assumed to construct the baseline availability scenario for the numerical case study. The corresponding transition and recovery rates are then derived from these characteristic times according to $\lambda = 1/T$, where T denotes the assumed characteristic transition or recovery time. The available capacity coefficient is defined as the ratio of the available power under the derated state to the rated power and is specified as a representative degraded-state capacity assumption rather than a statistically calibrated value.

Table 2. Assumed parameters of the Markov-chain-based hydrogen equipment state model used in the numerical case study.

Parameter	Meaning	EL Value	HFC Value	Unit
λ_{01}	Normal to degraded transition rate	0.015	0.012	day^{-1}
λ_{02}	Normal to outage transition rate	0.003	0.004	day^{-1}
λ_{12}	Degraded to outage transition rate	0.012	0.01	day^{-1}
μ_{10}	Degraded recovery rate	0.12	0.1	day^{-1}
μ_{20}	Outage recovery rate	0.08	0.07	day^{-1}
μ_{21}	Outage to degraded recovery rate	0.1	0.09	day^{-1}
ρ	Available capacity coefficient in degraded state	0.6	0.7	–

Specifically, for the HFC, representative characteristic transition times of approximately 83.3, 250, and 100 days are assumed for the normal-to-degraded, normal-to-outage, and degraded-to-outage transitions, respectively. According to $\lambda = 1/T$, these assumptions yield the corresponding transition rates of 0.012, 0.004, and 0.010 day^{-1}. Similarly, representative recovery times of approximately 10, 14.3, and 11.1 days are assumed, resulting in recovery rates of 0.10, 0.07, and 0.09 day^{-1}, respectively.

For the EL (EL), representative characteristic transition times of approximately 66.7, 333.3, and 83.3 days are assumed, corresponding to transition rates of 0.015, 0.003, and 0.012 day^{-1}, respectively. Representative recovery times of approximately 8.3, 12.5, and 10 days are assumed, yielding recovery rates of 0.12, 0.08, and 0.10 day^{-1}, respectively.

The degraded-state available capacity coefficients are assumed to be 0.6 for the EL and 0.7 for the HFC, indicating that 60% and 70% of the rated capacity remain available under the degraded state, respectively. These values are adopted as representative baseline assumptions for the numerical case study rather than device-specific statistically calibrated reliability parameters.

The following assumptions are adopted for the multi-state Markov model:

(1) Hydrogen energy equipment is represented by three availability states, including normal operation, degraded operation, and outage.
(2) The state transition process satisfies the memoryless property of the Markov chain, where future state evolution depends only on the current state.
(3) Complete outage represents a zero available capacity state, while degraded operation corresponds to partial capacity availability.
(4) The recovery process is considered possible during the scheduling horizon, allowing the equipment to return from degraded or outage states to available states.

2.3. Source–Load–Storage Coordinated Operation Modeling Considering the Failure Probability of Hydrogen Energy Equipment

2.3.1. Thermal Power Unit Model

The operation of thermal power units must satisfy the power constraints, ramping-rate constraints, and other conditions:

$$u_t^{\mathrm{G}} P_{\min}^{\mathrm{G}} \le P_t^{\mathrm{G}} \le u_t^{\mathrm{G}} P_{\max}^{\mathrm{G}} \tag{6}$$

$$\Delta R_{\min}^{G} \le P_t^{G} - P_{t-1}^{G} \le \Delta R_{\max}^{G} \tag{7}$$

where P_t^{G} is the output of the thermal power unit; $P_{\max}^{\mathrm{G}}$ and $P_{\min}^{\mathrm{G}}$ are the upper and lower output limits of the thermal power unit, respectively; $\Delta R_{\max}^{\mathrm{G}}$ and $\Delta R_{\min}^{\mathrm{G}}$ are the upper and lower ramping-rate limits of the thermal power unit, respectively; and u_t^{G} is the start–stop variable of the thermal power unit.

2.3.2. Multi-Scenario Mathematical Model of Hydrogen Energy Storage Considering Failure Probability

The EL converts surplus wind power into hydrogen through water electrolysis and is a key device for power-to-gas conversion. In this paper, a proton exchange membrane EL is adopted. The electricity-to-hydrogen conversion relationship and operating power constraints of the EL are expressed as follows:

$$P_{\mathrm{H_2},t}^{\mathrm{EL}} = \eta^{\mathrm{EL}} P_{\mathrm{e},t}^{\mathrm{EL}} \tag{8}$$

$$0 \le P_{e,t}^{\mathrm{EL}} \le \overline{\alpha}^{\mathrm{EL}} \mu_t^{\mathrm{EL}} P_{e,\max}^{\mathrm{EL}} \tag{9}$$

where $P^{\mathrm{EL}}_{\mathrm{H}_2,t}$ is the chemical energy rate of the hydrogen produced by the EL, expressed on the higher heating value (HHV) basis; $P^{\mathrm{EL}}_{\mathrm{e},t}$ is the power consumption of the EL; η^{EL} is the electricity-to-hydrogen conversion efficiency on the HHV basis; μ^{EL}_t is the start–stop state variable of the EL; and $P^{\mathrm{EL}}_{e,\max}$ is the upper limit of the power consumption of the EL.

Under a fault condition, the nominal upper power limit of the EL is replaced by its state-dependent available capacity. Therefore, a derated state restricts the maximum electrical power that can be absorbed by the EL, whereas an outage state forces its operating power and corresponding hydrogen-production power to zero. This state-dependent capacity constraint establishes the link between the physical EL failure mechanism and the system-level scheduling model.

The HFC converts the chemical energy of hydrogen into electrical energy through the electrochemical reaction between hydrogen and oxygen and is a key device for realizing hydrogen-to-electricity conversion. The relationship between its output power and hydrogen-to-electricity conversion power is given as follows:

$$P^{\mathrm{HFC}}_{\mathrm{e},t} = \eta^{\mathrm{HFC}}_{\mathrm{e}} P^{\mathrm{HFC}}_{\mathrm{H}_2,t} \tag{10}$$

Meanwhile, the HFC is also subject to the joint constraints of the start–stop state and rated operating capacity, namely

$$0 \le P^{\mathrm{HFC}}_{\mathrm{H}_2,t} \le \overline{\alpha} \mu^{\mathrm{HFC}}_t P^{\mathrm{HFC}}_{\mathrm{H}_2,\max} \tag{11}$$

where $P^{\mathrm{HFC}}_{\mathrm{e},t}$ is the output power of the HFC; $P^{\mathrm{HFC}}_{\mathrm{H}_2,t}$ is the hydrogen power of the HFC; $\eta^{\mathrm{HFC}}_{\mathrm{e}}$ is the power generation efficiency of the HFC; μ^{HFC}_t is the start–stop state variable of the HFC; and $P^{\mathrm{HFC}}_{\mathrm{H}_2,\max}$ is the upper limit of the hydrogen consumption power of the HFC.

Furthermore, to describe the dynamic changes in the hydrogen storage system in different time periods, a hydrogen storage state equation is established. The hydrogen storage capacity is generally constrained by the hydrogen production of the EL, the hydrogen consumption of the HFC, and the hydrogen storage capacity, and its expression is

$$E^{\mathrm{H}}_t = (1-\tau^{\mathrm{H}}) E^{\mathrm{H}}_{t-1} + \eta^{\mathrm{H,ch}} P^{\mathrm{EL}}_{H_2,t} \Delta t - \frac{P^{\mathrm{HFC}}_{H_2,t} \Delta t}{\eta^{\mathrm{H,dis}}} \tag{12}$$

$$E^{\mathrm{H}}_{\min} \le E^{\mathrm{H}}_t \le E^{\mathrm{H}}_{\max} \tag{13}$$

$$E^{\mathrm{H}}_0 = E^{\mathrm{H}}_{24} \tag{14}$$

where E^{H}_t and E^{H}_{t-1} are the hydrogen storage amounts of the hydrogen energy storage system in periods t and $t-1$, respectively; τ^{H} is the self-loss rate of the hydrogen energy storage system; $\eta^{\mathrm{H,ch}}$ is the hydrogen charging efficiency of the hydrogen energy storage system; $\eta^{\mathrm{H,dis}}$ is the hydrogen discharging efficiency of the hydrogen energy storage system; $E^{\mathrm{H}}_{\min}$ and $E^{\mathrm{H}}_{\max}$ are the lower and upper limits of the hydrogen storage capacity of the hydrogen energy storage system, respectively; E^{H}_0 and E^{H}_{24} are the hydrogen storage amounts at 0:00 and 24:00, respectively; and Δt is the scheduling time interval.

2.3.3. Electrical Energy Storage System Model

The ESS can improve system flexibility by providing short-term power regulation and energy shifting. Its operating state is characterized by the stored energy, charging and

discharging power, self-discharge rate, and charging/discharging efficiencies. The ESS model is expressed as follows:

$$\begin{cases} E_t^{\mathrm{ES}} = E_{t-1}^{\mathrm{ES}}(1-\tau) + \eta_{\mathrm{c}}^{\mathrm{ES}} P_{\mathrm{c},t}^{\mathrm{ES}} \Delta t - \frac{P_{\mathrm{d},t}^{\mathrm{ES}} \Delta t}{\eta_{\mathrm{d}}^{\mathrm{ES}}} \\ E_{\min}^{\mathrm{ES}} \le E_t^{\mathrm{ES}} \le E_{\max}^{\mathrm{ES}} \\ E_0^{\mathrm{ES}} = E_{24}^{\mathrm{ES}} \end{cases} \tag{15}$$

where E_t^{ES} is the energy storage capacity in period t; τ is the self-discharge rate of the energy storage; $\eta_{\mathrm{c}}^{\mathrm{ES}}$ and $\eta_{\mathrm{d}}^{\mathrm{ES}}$ are the charging and discharging efficiencies of the energy storage, respectively; $P_{\mathrm{c},t}^{\mathrm{ES}}$ and $P_{\mathrm{d},t}^{\mathrm{ES}}$ are the charging and discharging powers in period t, respectively; $E_{\min}^{\mathrm{ES}}$ and $E_{\max}^{\mathrm{ES}}$ are the lower and upper limits of the energy storage capacity, respectively; and E_0^{ES} and E_{24}^{ES} are the energy storage capacities at 0:00 and 24:00, respectively.

2.3.4. Load Model

Since user-side loads are not completely rigid, part of the electricity demand is adjustable and has a certain degree of regulability. Through price incentives or dispatching compensation, demand response resources can actively participate in operation regulation during periods of tight system supply, insufficient renewable energy output, or large peak–valley differences, thereby alleviating power and energy balance pressure. This paper focuses on the coordinated role of multiple source–load–storage resources in power and energy balance, rather than the detailed classification behavior of different response types on the user side. Therefore, to aggregate demand response resources such as adjustable loads,

$$0 \le P_t^{\mathrm{DR}} \le \alpha_{\max}^{\mathrm{DR}} P_t^{\mathrm{L}} \tag{16}$$

$$\sum_{t \in T} P_t^{\mathrm{DR}} \Delta t \;\; \le \;\; E_{\max}^{\mathrm{DR}} \tag{17}$$

where P_t^{DR} is the load reduction power of demand response in period t; $\alpha_{\max}^{\mathrm{DR}}$ is the maximum allowable reduction ratio of demand response; P_t^{L} is the original load power in period t; and $E_{\max}^{\mathrm{DR}}$ is the maximum load energy allowed to be reduced within one scheduling cycle.

When the generating units in the system cannot meet the load demand, electricity needs to be purchased from the distribution network; otherwise, the system can sell surplus electricity to the distribution network to obtain revenue. In addition, considering that the system in this paper is equipped with multiple flexible resources such as ELs, energy storage, and grid interaction, surplus renewable energy can be accommodated through hydrogen production by electrolysis, energy storage charging, or electricity sales to the external grid. Therefore, this paper no longer separately sets wind and photovoltaic curtailment variables, and the wind and photovoltaic outputs both represent the renewable energy power actually accommodated by the system.

The power and energy balance constraint of the system is as follows:

$$P_t^{\mathrm{G}} + P_t^{\mathrm{WT}} + P_t^{\mathrm{PV}} + P_t^{\mathrm{HFC}} + P_t^{\mathrm{ES,dis}} + P_t^{\mathrm{buy}} = P_t^{\mathrm{L}} - P_t^{\mathrm{DR}} + P_t^{\mathrm{EL}} + P_t^{\mathrm{ES,ch}} + P_t^{\mathrm{sell}} \tag{18}$$

where P_t^{buy} and P_t^{sell} are the powers purchased from and sold to the distribution network by the system in period t, respectively.

2.4. Hierarchical Multi-Time-Scale Low-Carbon Rolling Optimization Model Considering the Uncertainty of Medium- and Long-Term Plan Decomposition

Multi-time-scale scheduling methods that combine day-ahead optimization with intra-day MPC correction have been shown to improve operational adaptability under renewable generation and load uncertainty [26]. Inspired by this idea, this paper constructs

a hierarchical multi-time-scale optimization model combining stochastic decomposition of medium- and long-term plans, day-ahead two-stage stochastic optimization, and intra-day MPC rolling correction. The medium- and long-term layer takes the month as the basic time unit and decomposes the power generation task and total carbon budget within the cycle into each operating day; the day-ahead layer formulates a 24 h benchmark operation plan according to the decomposition results of the upper layer and describes short-term uncertainty through wind–solar–hydrogen joint scenarios; and the intra-day layer performs rolling correction on the day-ahead plan according to real-time states and updated forecasts.

2.4.1. Dynamic Carbon Quota and Carbon Trading Model

Carbon allowance allocation has an important influence on low-carbon dispatch results. Existing studies have shown that, compared with fixed carbon allowance settings, multi-time-scale allocation of carbon allowances can better coordinate long-term emission budgets and short-term operational decisions in integrated energy systems [16]. Inspired by this idea, this paper further constructs a dynamic carbon quota mechanism to reflect the influence of load level, renewable energy output, and hydrogen energy equipment operating state on the allocation of carbon emission responsibility under different dispatching periods.

In this study, the carbon budget refers to the daily emission target issued by the medium- and long-term scheduling layer, the carbon quota refers to the time-varying emission limit allocated to each dispatch period, and the carbon allowance refers to the tradable emission right purchased from or sold to the carbon market.

The system dynamic carbon quota allocated to each dispatch period is expressed as follows:

$$Q_{d,t}^{\mathrm{dyn}} = Q_{d}^{\mathrm{target}} \frac{\omega_{d,t} \hat{P}_{d,t}^{\mathrm{L}} \Delta t}{\sum_{\tau} \omega_{d,\tau} \hat{P}_{d,\tau}^{\mathrm{L}} \Delta t} \tag{19}$$

where Q_{d}^{target} is the daily carbon emission budget obtained by decomposing the medium- and long-term layer on day d; $\hat{P}_{d,t}^{\mathrm{L}}$ is the predicted load in period t under day-ahead scenario s; and $\omega_{d,t}$ is the dynamic quota weight, which is used to characterize the influence of the system operating state on carbon quota allocation.

$$\omega_{d,t} = 1 + \alpha_{\mathrm{L}} \widetilde{L}_{d,t} - \alpha_{\mathrm{R}} \widetilde{R}_{d,t} + \alpha_{\mathrm{H}} \widetilde{F}_{d,t} \tag{20}$$

where $\widetilde{L}_{d,t}$ is the normalized load level; $\widetilde{R}_{d,t}$ is the normalized renewable energy penetration rate; $\widetilde{F}_{d,t}$ is the unavailability risk indicator of hydrogen energy equipment; and α_{L}, α_{R}, and α_{H} are the influence coefficients of load level, renewable energy penetration rate, and equipment state on the dynamic carbon quota, respectively. This mechanism ensures that the total daily carbon emission budget remains unchanged while realizing the dynamic allocation of quotas among different operating periods. α_{L} is empirically set to 0.25. α_{L}, α_{R}, and α_{H} are set to 0.25, 0.30, and 0.20, respectively.

According to the carbon emission accounting boundary defined in Section 2.1, operational CO_2 emissions are attributed to thermal power generation and electricity imported from the external grid. For the day-ahead scheduling model, one day is divided into 24 hourly periods, with Δt = 1 h. The electricity consumption of ESS and hydrogen energy conversion/storage processes is included in the system power and energy balance through

the corresponding power and efficiency terms. Therefore, the operational carbon emissions within one day can be expressed as follows:

$$C^{\text{emi}} = \sum_{t=1}^{24} (\delta P_t^{\text{G}} + \delta^{\text{grid}} P_t^{\text{buy}}) \Delta t \tag{21}$$

$$C^{\text{emi}} - Q^{\text{dyn}} = B^{\text{CO}_2,\text{buy}} - B^{\text{CO}_2,\text{sell}} \tag{22}$$

where C^{emi} denotes the total actual carbon emissions within the scheduling cycle, and δ is the carbon emission coefficient of the thermal power unit; $B^{\text{CO}_2,\text{buy}}$ denotes the amount of carbon emission allowances to be purchased; $B^{\text{CO}_2,\text{sell}}$ denotes the amount of carbon emission allowances available for sale. In this study, δ is set to 0.8 kgCO_2/kWh [33] and δ^{grid} is set to 0.5366 kgCO_2/kWh [34]. The former represents the operational emission intensity of thermal power generation, whereas the latter represents the emission intensity associated with electricity imported from the external grid. These values are adopted as representative baseline parameters for the synthetic test system under the operational carbon-accounting boundary defined in Section 2.1, rather than as universally applicable emission factors.

Therefore, the carbon emission cost model can be obtained as follows:

$$C_d^{\text{carbon}} = \lambda^{\text{CO}_2} \left(B_d^{\text{CO}_2,\text{buy}} - B_d^{\text{CO}_2,\text{sell}} \right) \tag{23}$$

where λ^{CO_2} is the carbon trading price. It should be noted that when the actual carbon emissions are higher than the dynamic carbon quota, the system needs to purchase carbon emission allowances in the carbon trading market; when the actual carbon emissions are lower than the dynamic carbon quota, the system can sell the surplus carbon allowances to obtain revenue.

2.4.2. Medium- and Long-Term Stochastic Decomposition Model

The role of the medium- and long-term layer is to reasonably decompose the periodic power generation task and total carbon budget into each operating day under the uncertainty of future load, wind–photovoltaic output, electricity price, and hydrogen energy equipment availability.

The medium- and long-term stochastic decomposition model aims to minimize the sum of the benchmark planning cost and the scenario-expected adjustment cost:

$$minF^{\text{UL}} = \sum_{d \in D} c^{\text{G}} E_d^0 + \sum_{\omega \in \Omega^{\text{ML}}} \pi_\omega \sum_{d \in D} C_{d,\omega}^{\text{adj}} \tag{24}$$

where D is the set of dates within the medium- and long-term planning period; c^{G} is the unit cost of the benchmark power generation on day d; E_d^0 is the benchmark power generation on day d; π_ω is the probability of scenario ω; and $C_{d,\omega}^{\text{adj}}$ is the adjustment cost under scenario ω on day d.

The scenario adjustment cost includes the power generation adjustment cost, carbon budget adjustment cost, demand response compensation cost, and carbon trading cost:

$$C_{d,\omega}^{\text{adj}} = C_{d,\omega}^{\text{E}} + C_{d,\omega}^{\text{Q}} + C_{d,\omega}^{\text{DR,ML}} + C_{d,\omega}^{\text{carbon,ML}} \tag{25}$$

Among them, the power generation adjustment cost is used to reflect the upward or downward adjustment cost of the power generation task on day d under scenario ω relative to the benchmark plan, which is expressed as follows:

$$C_{d,\omega}^{\mathrm{E}} = c^{\mathrm{E},+}\Delta E_{d,\omega}^{+} \quad + \quad c^{\mathrm{E},-}\Delta E_{d,\omega}^{-} \tag{26}$$

where $c^{\mathrm{E},+}$ and $c^{\mathrm{E},-}$ are the unit adjustment costs for upward and downward power generation adjustment on day d, respectively; $\Delta E_{d,\omega}^{+}$ and $\Delta E_{d,\omega}^{-}$ are the upward and downward power generation adjustment amounts on day d under scenario ω, respectively.

Similarly, the carbon budget adjustment cost is used to characterize the correction cost of the dynamic carbon budget under uncertain scenarios, which is expressed as follows:

$$C_{d,\omega}^{\mathrm{Q}} = c_{d}^{\mathrm{Q},+}\Delta Q_{d,\omega}^{+} \quad + \quad c_{d}^{\mathrm{Q},-}\Delta Q_{d,\omega}^{-} \tag{27}$$

where $c_{d}^{\mathrm{Q},+}$ and $c_{d}^{\mathrm{Q},-}$ are the unit adjustment costs for upward and downward carbon budget adjustment on day d, respectively; $\Delta Q_{d,\omega}^{+}$ and $\Delta Q_{d,\omega}^{-}$ are the upward and downward carbon budget adjustment amounts on day d under scenario ω, respectively.

In addition, to compensate for the loss of electricity consumption comfort caused by user-side load regulation, the demand response compensation cost is introduced:

$$C_{d,\omega}^{\mathrm{DR,ML}} = c^{\mathrm{DR}} E_{d,\omega}^{\mathrm{DR,ML}} \tag{28}$$

where c^{DR} is the unit demand response compensation cost; $E_{d,\omega}^{\mathrm{DR,ML}}$ is the demand response electricity on day d under scenario ω in the medium- and long-term layer.

Finally, the deviation between actual carbon emissions and the dynamic carbon quota is characterized by the carbon trading cost, which is calculated according to the carbon trading model shown in Equation (29).

To ensure that the total medium- and long-term power generation task is fully decomposed within the planning period and to characterize the power generation task and carbon budget under uncertain scenarios.

$$\sum_{d \in \mathcal{D}} E_{d}^{0} = E^{\mathrm{ML}} \tag{29}$$

$$\widetilde{E}_{d,\omega} = E_{d}^{0} + \Delta E_{d,\omega}^{+} - \Delta E_{d,\omega}^{-} \tag{30}$$

$$\sum_{d} \widetilde{E}_{d,\omega} = E^{\mathrm{ML}} \tag{31}$$

$$\sum_{d \in D} Q_{d}^{0} = Q^{\mathrm{ML}} \tag{32}$$

$$\widetilde{Q}_{d,\omega} = Q_{d}^{0} + \Delta Q_{d,\omega}^{+} - \Delta Q_{d,\omega}^{-} \tag{33}$$

$$\sum_{d} \widetilde{Q}_{d,\omega} = Q^{\mathrm{ML}} \tag{34}$$

where E^{ML} is the total power generation task within the medium- and long-term planning period; $\widetilde{E}_{d,\omega}$ is the corrected power generation task on day d under scenario ω; Q_{d}^{0} is the benchmark carbon budget on day d; Q^{ML} is the total carbon budget within the medium- and long-term planning period; and $\widetilde{Q}_{d,\omega}$ is the corrected daily carbon budget on day d under scenario ω.

The daily-scale electricity balance under each scenario is

$$\overset{\sim G,\mathrm{ML}}{E}_{d,\omega} + E_{d,\omega}^{\mathrm{WT,ML}} + E_{d,\omega}^{\mathrm{PV,ML}} + E_{d,\omega}^{\mathrm{buy,ML}} = E_{d,\omega}^{\mathrm{L,ML}} - E_{d,\omega}^{\mathrm{DR,ML}} + E_{d,\omega}^{\mathrm{sell,ML}} \tag{35}$$

where $\overset{\sim G,\mathrm{ML}}{E}_{d,\omega}$ is the corrected thermal power generation on day d under scenario ω; $E_{d,\omega}^{\mathrm{WT,ML}}$ and $E_{d,\omega}^{\mathrm{PV,ML}}$ are the actual accommodated wind and photovoltaic energy on day d under scenario ω, respectively; $E_{d,\omega}^{\mathrm{buy,ML}}$ and $E_{d,\omega}^{\mathrm{sell,ML}}$ are the electricity purchased from and sold to the external grid on day d under scenario ω, respectively; $E_{d,\omega}^{\mathrm{L,ML}}$ is the load demand energy on day d under scenario ω; and $E_{d,\omega}^{\mathrm{DR,ML}}$ is the demand response reduction energy on day d under scenario ω. This equation is used to ensure the daily-scale electricity balance of the medium- and long-term decomposition layer under different uncertain scenarios.

2.4.3. Day-Ahead Two-Stage Stochastic Low-Carbon Optimization Model

The day-ahead layer formulates a 24 h benchmark dispatch plan according to the daily power generation task and daily carbon budget provided by the medium- and long-term layer, and characterizes wind–photovoltaic forecast errors and the uncertainty of hydrogen energy equipment operating states through short-term scenarios. The first-stage variables of the day-ahead two-stage model include the unit start–stop state, day-ahead thermal power output, reserve capacity, and day-ahead contracted wind–photovoltaic power:

$$x_d = \left\{ u_{d,t}, P_{d,t}^{\mathrm{G,DA}}, R_{d,t}^{+}, R_{d,t}^{-} \right\} \tag{36}$$

The second-stage scenario recourse variables include reserve deployment, energy storage charging and discharging, electricity purchasing and selling, and demand response:

$$y_{d,s} = \left\{ r_{d,t,s}^{+}, r_{d,t,s}^{-}, P_{d,t,s}^{\mathrm{ES,ch}}, P_{d,t,s}^{\mathrm{ES,dis}} P_{e,d,t,s}^{\mathrm{EL}}, P_{e,d,t,s}^{\mathrm{HFC}}, P_{d,t,s}^{\mathrm{buy}}, P_{d,t,s}^{\mathrm{sell}}, P_{d,t,s}^{\mathrm{DR}} \right\} \tag{37}$$

Under scenario s, the actual dispatch output of the thermal power unit satisfies the reserve dispatch constraint:

$$0 \le r_{d,t,s}^{+} \le R_{d,t}^{+} \tag{38}$$

$$0 \le r_{d,t,s}^{-} \le R_{d,t}^{-} \tag{39}$$

$$P_{d,t}^{\mathrm{G}} = P_{d,t}^{\mathrm{G,DA}} + r_{d,t,s}^{+} - r_{d,t,s}^{-} \tag{40}$$

$$P_{d,t}^{\mathrm{G,DA}} + R_{d,t}^{+} \le u_{d,t}^{G} P_{\max}^{\mathrm{G}} \tag{41}$$

$$P_{d,t}^{\mathrm{G,DA}} - R_{d,t}^{-} \ge u_{d,t}^{G} P_{\min}^{\mathrm{G}} \tag{42}$$

where $r_{d,t,s}^{+}$ and $r_{d,t,s}^{-}$ are the upward and downward reserve actually deployed in period t under scenario s, respectively; $R_{d,t}^{+}$ and $R_{d,t}^{-}$ are the upward and downward reserve capacities reserved day-ahead, respectively; and $P_{d,t}^{\mathrm{G,DA}}$ is the day-ahead scheduled output of the thermal power unit in period t.

The objective of the day-ahead two-stage model is to minimize the sum of the first-stage planning cost, the second-stage scenario-expected recourse cost, and the medium- and long-term task tracking penalty cost:

$$\min C_d^{(1)}(x_d) + \sum_{s \in S_d^{\mathrm{DA}}} \pi_{d,s} C_{d,s}^{(2)}(x_d, y_{d,s}) + C_d^{\mathrm{track}} \tag{43}$$

The first-stage cost includes the start-up and shutdown costs and reserve costs:

$$C_d^{(1)} = \sum_{t \in T_d} \left(c^{\mathrm{SU}} y_{d,t}^{\mathrm{on}} + c^{\mathrm{SD}} y_{d,t}^{\mathrm{off}} + c^{\mathrm{R},+} R_{d,t}^{+} + c^{\mathrm{R},-} R_{d,t}^{-} \right) \tag{44}$$

$$y_{d,t}^{\mathrm{on}} \geq u_{d,t} - u_{d,t-1} \tag{45}$$

$$y_{d,t}^{\mathrm{off}} \geq u_{d,t-1} - u_{d,t} \tag{46}$$

where $\pi_{d,s}$ denotes the occurrence probability of scenario s; c^{SU} and c^{SD} are the start-up and shutdown cost coefficients of the thermal power unit, respectively; and $y_{d,t}^{\mathrm{on}}$ and $y_{d,t}^{\mathrm{off}}$ are the start-up and shutdown state variables of the thermal power unit in period t on day d, respectively.

The second-stage scenario-expected recourse cost consists of the thermal power unit operating cost, demand response compensation cost, external grid interaction cost, and carbon trading cost:

$$C_{d,s}^{(2)} = \sum_{t \in T_d} \left[a \left(P_{d,t,s}^{\mathrm{G}} \right)^2 + b P_{d,t,s}^{\mathrm{G}} + c u_{d,t} \right] \Delta t + C_{d,s}^{\mathrm{DR}} + C_{d,s}^{\mathrm{grid}} + C_{d,s}^{\mathrm{carbon}} \tag{47}$$

where

$$C_{d,s}^{\mathrm{DR}} = \sum_{t \in T_d} c^{\mathrm{DR}} P_{d,t,s}^{\mathrm{DR}} \Delta t \tag{48}$$

$$C_{d,s}^{\mathrm{grid}} = \sum_{t \in T_d} \lambda_t \left(P_{d,t,s}^{\mathrm{buy}} - P_{d,t,s}^{\mathrm{sell}} \right) \Delta t \tag{49}$$

$$C_{d,s}^{\mathrm{carbon}} = \lambda^{\mathrm{CO_2}} \left(C_{d,s}^{\mathrm{emi}} - Q_{d,s}^{\mathrm{dyn}} \right) \tag{50}$$

$$C_{d,s}^{\mathrm{emi}} = \sum_{t \in T_d} \delta P_{d,t,s}^{\mathrm{G}} \Delta t \tag{51}$$

$$Q_{d,s}^{\mathrm{dyn}} = \sum_{t \in T_d} Q_{d,t,s}^{\mathrm{dyn}} \tag{52}$$

To further ensure that the day-ahead scheduling results can accommodate the daily power generation task and daily carbon emission budget decomposed and issued by the medium- and long-term layer, this paper introduces task tracking constraints and corresponding deviation variables to quantify the deviation between the day-ahead plan and the upper-layer decomposition targets.

$$\sum_{t \in T_d} P_t^{\mathrm{G,DA}} \Delta t + \varepsilon_d^{\mathrm{E},-} - \varepsilon_d^{\mathrm{E},+} = E_d^{\mathrm{DA}} \tag{53}$$

$$\sum_{s \in S_d^{\mathrm{DA}}} \pi_{d,s} C_{d,s}^{\mathrm{emi}} \leq Q_d^{\mathrm{DA}} + \varepsilon_d^{\mathrm{Q},+} \tag{54}$$

The medium- and long-term task tracking penalty cost is expressed as:

$$C_d^{\mathrm{track}} = \left(\rho^{\mathrm{E},+} \varepsilon_d^{\mathrm{E},+} + \rho^{\mathrm{E},-} \varepsilon_d^{\mathrm{E},-} \right) + \rho^{\mathrm{Q}} \varepsilon_d^{\mathrm{Q},+} \tag{55}$$

where $P_t^{\mathrm{G,DA}}$ denotes the unit output at time period t in the day-ahead scheduling; E_d^{DA} denotes the power generation task decomposed by the medium- and long-term layer for day d; $\varepsilon_d^{\mathrm{E},+}$ and $\varepsilon_d^{\mathrm{E},-}$ denote the positive and negative deviations of the day-ahead generation plan from the daily generation task, respectively; Q_d^{DA} denotes the carbon emission budget decomposed by the medium- and long-term layer for day d; $\varepsilon_d^{\mathrm{Q},+}$ denotes the deviation

amount by which carbon emissions exceed the budget; and $\rho^{E,+}$, $\rho^{E,-}$ and ρ^{Q} denote the penalty coefficients corresponding to the respective deviation variables.

It should be noted that the task tracking penalty is an auxiliary optimization term used to enforce the generation-task and carbon budget tracking requirements. It does not represent an actual monetary expenditure and is therefore excluded when calculating the total system operating cost reported in Section 3.3.

2.4.4. Intra-Day MPC Rolling Correction Model

Model predictive control (MPC) has been widely applied in microgrid and integrated energy system operation because its receding-horizon optimization and feedback-correction mechanism can update control decisions according to refreshed forecasts and observed system states. Therefore, in this paper, MPC is adopted in the intra-day layer to correct deviations from the day-ahead schedule and to continuously track the remaining generation task and carbon emission budget.

Specifically, the intra-day layer performs rolling optimization at rolling time k according to the actual results already obtained and the latest forecast information. Before rolling time k, the actual generated energy that has been completed on the current day is

$$E_{d,k}^{\mathrm{act}} = \sum_{\tau=1}^{k-1} P_{d,\tau}^{\mathrm{G,act}} \Delta t \tag{56}$$

The actual carbon emissions that have been generated before rolling time k are

$$C_{d,k}^{\mathrm{emi,act}} = \sum_{\tau=1}^{k-1} \delta P_{d,\tau}^{\mathrm{G,act}} \Delta t \tag{57}$$

where the remaining power generation task of the current day is

$$E_{d,k}^{\mathrm{re}} = E_{d}^{\mathrm{target}} - E_{d,k}^{\mathrm{act}} \tag{58}$$

and the remaining carbon budget of the current day is

$$Q_{d,k}^{\mathrm{re}} = Q_{d}^{\mathrm{target}} - C_{d,k}^{\mathrm{emi,act}} \tag{59}$$

where $E_{d,k}^{\mathrm{act}}$ denotes the actual generated energy completed before rolling time k on day d; $P_{d,\tau}^{\mathrm{G,act}}$ denotes the actual unit output at time period τ on day d; $C_{d,k}^{\mathrm{emi,act}}$ denotes the actual carbon emissions generated before rolling time k on day d; E_{d}^{target} and Q_{d}^{target} denote the daily power generation target and daily carbon emission budget, respectively; and $E_{d,k}^{\mathrm{re}}$ and $Q_{d,k}^{\mathrm{re}}$ denote the remaining power generation task and remaining carbon emission budget after rolling time k, respectively.

To ensure that the daily power generation task and daily carbon budget obtained from the medium- and long-term decomposition can be continuously tracked in the intra-day execution process, this paper introduces remaining task tracking constraints into the intra-day MPC model. According to the actual generated energy and actual carbon emissions completed before rolling time k, the model calculates the remaining power generation task and remaining carbon budget of the current day and tracks them within the current rolling optimization time domain.

$$\sum_{\tau=k}^{T} P_{d,\tau|k}^{\mathrm{G,MPC}} \Delta t + \varepsilon_{d,k}^{\mathrm{E},-} - \varepsilon_{d,k}^{\mathrm{E},+} = E_{d,k}^{\mathrm{re}} \tag{60}$$

$$\sum_{\tau=k}^{T} \delta P_{d,\tau|k}^{\mathrm{G,MPC}} \Delta t \;\leq\; Q_{d,k}^{\mathrm{re}} + \varepsilon_{d,k}^{\mathrm{Q},+} \tag{61}$$

The MPC rolling optimization objective function is

$$\min C_{d,k}^{\mathrm{MPC}} + \rho_p \sum_{\tau=k}^{k+N-1} \left(P_{d,\tau\,|\,k}^{\mathrm{G,MPC}} - P_{d,\tau}^{\mathrm{G,DA}*} \right)^2 + \rho^{\mathrm{E},+} \varepsilon_{d,k}^{\mathrm{E},+} + \rho^{\mathrm{E},-} \varepsilon_{d,k}^{\mathrm{E},-} + \rho^{\mathrm{Q}} \varepsilon_{d,k}^{\mathrm{Q},+} \tag{62}$$

where $C_{d,k}^{\mathrm{MPC}}$ denotes the operating cost of the MPC rolling optimization; ρ_p is the penalty coefficient for day-ahead plan tracking; $P_{d,\tau|k}^{\mathrm{G,MPC}}$ denotes the unit output at time period τ optimized by the MPC model at rolling time k on day d; and $P_{d,\tau}^{\mathrm{G,DA}*}$ denotes the optimal unit output obtained from the day-ahead scheduling model.

On the basis of the above objective function and remaining task tracking constraints, the intra-day MPC model also needs to satisfy real-time power and energy balance constraints, thermal power unit output and ramping constraints, energy storage operation constraints, hydrogen energy equipment operation constraints, demand response constraints, and remaining carbon budget constraints. The basic forms of the above constraints are consistent with those of the day-ahead two-stage model, but the day-ahead scenario variables need to be replaced by variables updated based on the latest forecast information within the rolling horizon, and the actual equipment state at rolling time k is used as the initial condition. According to the MPC rolling optimization mechanism, only the dispatching result of the current time period is implemented in each optimization, and then the model enters the next rolling time according to the new actual operating state and forecast information. Compared with the day-ahead model, the intra-day MPC model not only corrects the deviation of the day-ahead power plan, but also explicitly tracks the daily power generation task and daily carbon budget decomposed by the upper layer, thereby realizing feedback correction of the medium- and long-term plan during the intra-day execution stage.

To quantitatively evaluate the power deviation correction performance of the intra-day MPC, the power imbalance before correction at rolling instant k is first defined based on the realized load and renewable-power conditions, the available operating states of the hydrogen energy equipment, and the day-ahead dispatch plan. A positive deviation represents a power deficit, whereas a negative deviation represents a power surplus. The pre-correction power deviation is expressed as

$$\begin{aligned} \Delta P_k^{\mathrm{pre}} = &\left(P_k^{\mathrm{L}} - P_k^{\mathrm{DR,pre}} + P_k^{\mathrm{EL,pre}} + P_k^{\mathrm{ES,ch,pre}} + P_k^{\mathrm{sell,pre}} \right) \\ &- \left(P_k^{\mathrm{G,pre}} + P_k^{\mathrm{WT}} + P_k^{\mathrm{PV}} + P_k^{\mathrm{HFC,pre}} + P_k^{\mathrm{ES,dis,pre}} + P_k^{\mathrm{buy,pre}} \right) \end{aligned} \tag{63}$$

In particular, $P_k^{\mathrm{EL,pre}}$ and $P_k^{\mathrm{HFC,pre}}$ represent the feasible EL consumption and fuel-cell output under the actual equipment availability state at rolling instant k.

The total compensation provided by the flexible resources during the current MPC correction is defined as the net change in controllable power relative to the pre-correction operating point:

$$\begin{aligned} \Delta P_k^{\mathrm{comp}} = &\left(P_k^{G,\mathrm{MPC}} - P_k^{G,\mathrm{pre}} \right) + \left(P_k^{HFC,\mathrm{MPC}} - P_k^{HFC,\mathrm{pre}} \right) + \\ &\left[\left(P_k^{ES,dis,\mathrm{MPC}} - P_k^{ES,ch,\mathrm{MPC}} \right) - \left(P_k^{ES,dis,\mathrm{pre}} - P_k^{ES,ch,\mathrm{pre}} \right) \right] + \\ &\left[\left(P_k^{buy,\mathrm{MPC}} - P_k^{sell,\mathrm{MPC}} \right) - \left(P_k^{buy,\mathrm{pre}} - P_k^{sell,\mathrm{pre}} \right) \right] + \\ &\left(P_k^{DR,\mathrm{MPC}} - P_k^{DR,\mathrm{pre}} \right) - \left(P_k^{EL,\mathrm{MPC}} - P_k^{EL,\mathrm{pre}} \right) \end{aligned} \tag{64}$$

A positive ΔP_k^{comp} indicates that the coordinated resources compensate for a power deficit or reduce excess demand, whereas a negative value represents compensation in the opposite direction.

Accordingly, the residual power deviation after the current MPC correction is

$$e_k = \Delta P_k^{\text{pre}} - \Delta P_k^{\text{comp}} \tag{65}$$

This definition ensures that the residual deviation directly reflects the portion of the pre-correction imbalance that remains uncompensated after coordinated adjustment of thermal generation, electrical storage, hydrogen energy equipment, demand response, and grid interaction.

The overall power tracking performance over the complete intra-day scheduling horizon is evaluated using the root mean square error (RMSE):

$$\text{RMSE} = \sqrt{\frac{1}{N}\sum_{k=1}^{N} e_k^2} \tag{66}$$

where N is the total number of intra-day control intervals. In this study, the intra-day scheduling interval is 15 min and the 24 h horizon therefore contains $N = 96$ implemented MPC intervals.

After the daily dispatch is completed, the actual power generation and actual carbon emissions of the day are calculated and fed back to the medium- and long-term layer to update the remaining tasks of subsequent periods. After the end of day d, the calculated actual power generation and actual carbon emissions are

$$E_d^{\text{act}} = \sum_{t \in T_d} P_{d,t}^{\text{G,act}} \Delta t \tag{67}$$

$$C_d^{\text{emi,act}} = \sum_{t \in T_d} \delta P_{d,t}^{\text{G,act}} \Delta t \tag{68}$$

The above statistics reflect the actual execution results of intra-day dispatch on day d and serve as the basis for subsequent task correction in the medium- and long-term layer. By subtracting the actual completed amounts of the current day and previous operating days from the total medium- and long-term tasks, the remaining power generation task and remaining carbon emission budget to be completed in subsequent periods can be obtained.

$$E_d^{\text{re}} = E^{\text{ML}} - \sum_{\tau=1}^{d} E_\tau^{\text{act}} \tag{69}$$

$$Q_d^{\text{re}} = Q^{\text{ML}} - \sum_{\tau=1}^{d} C_\tau^{\text{emi,act}} \tag{70}$$

3. Results

3.1. Basic Data and Typical Scenario Generation

This paper considers a representative source–load–storage coordinated operation system as the case-study object and constructs a multi-time-scale optimal scheduling model including an equivalent thermal generation unit, wind power, photovoltaic power, ESS, hydrogen energy storage, and demand response resources, while considering power interaction with the external distribution network. Since the case study is constructed as a synthetic representative system rather than a specific real-world power system, the equipment capacities are configured according to the overall source–load scale and the required

coordination among multiple flexibility resources. The technical operating parameters are selected as representative values with reference to Refs. [35–41]. The main operating parameters of various devices are shown in Table 3.

Table 3. Main operating parameters of equipment.

Equipment	Parameter	Value	Unit
Equivalent thermal generation unit	Minimum output	50	kW
	Maximum output	1500	kW
ESS	Maximum charging/discharging power	400	kW
	Charging/discharging efficiency	0.98	—
EL	Rated power	1000	kW
	EL energy conversion efficiency, HHV basis	0.8	—
HFC	Hydrogen-to-electricity conversion efficiency, HHV basis	0.45	—
Hydrogen storage tank	Hydrogen energy storage capacity	2000	kWh (HHV basis)

A synthetic case-study dataset was constructed for a representative source–load–storage system to evaluate the proposed optimization method under controlled and reproducible operating conditions. Considering the seasonal variations in renewable generation, the WT and PV datasets were extended to 365 consecutive days with hourly resolution, resulting in 8760 data points for each renewable source. The annual renewable-power profiles incorporate representative intra-annual variations in output levels and daily generation characteristics. The data were constructed to reproduce the main operating characteristics relevant to the present study rather than to represent a specific power system or geographical location.

The load profile exhibits a typical daily peak–valley pattern, with relatively low demand during nighttime and higher demand during daytime and evening peak periods. WT power is characterized by continuous but stochastic fluctuations with seasonal variations in its overall output level, whereas PV power presents pronounced diurnal and seasonal variations, with zero output during nighttime and a daytime peak. The magnitudes of the load, WT, and PV profiles were coordinated with the capacity configuration of the test system to ensure physically feasible power-balance conditions.

Before being used in the optimization model, the load, WT, and PV time-series were aligned on a common 1 h time grid and checked against their corresponding operating ranges. No additional temporal interpolation was required because all input series were generated at the hourly resolution used by the day-ahead scheduling model. For renewable energy uncertainty modeling, the annual WT and PV power series were used as the basis for Monte Carlo scenario generation. Monte Carlo sampling was then employed to generate 500 joint WT–PV power scenarios, followed by K-means clustering of the normalized joint WT–PV scenario vectors to reduce the original scenario set to five representative scenarios for stochastic optimization.

The resulting annual WT and PV power profiles are shown in Figure 2, exhibiting both short-term stochastic fluctuations and seasonal variations over the annual cycle.

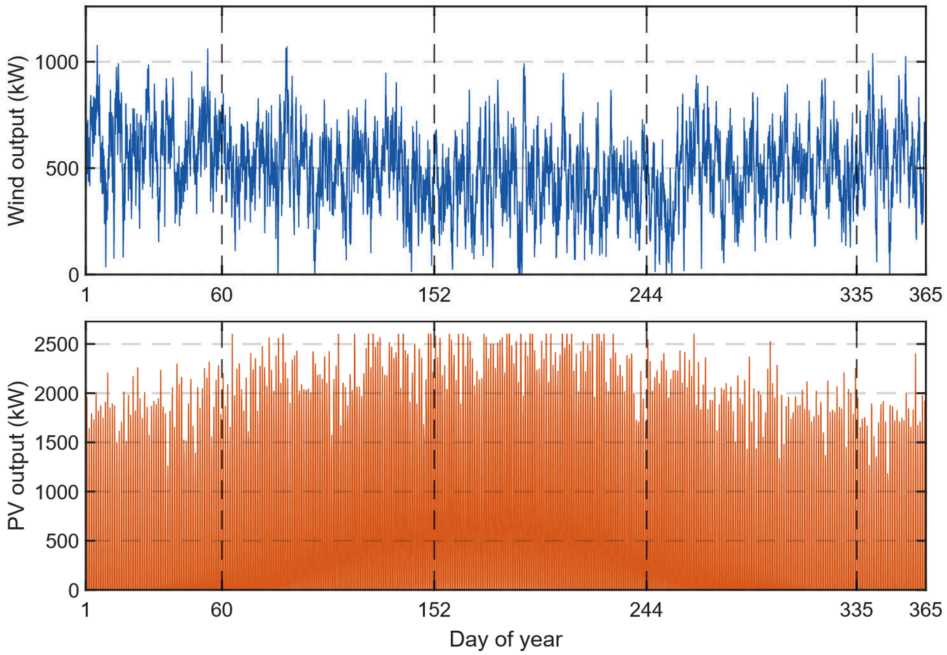


Figure 2. Annual synthetic renewable-power profiles.

It should be noted that fuel-cell power is not included as an exogenous time-series dataset. Instead, the fuel-cell output is an endogenous decision variable determined by the optimization model according to the hydrogen storage state, hydrogen-to-electricity conversion efficiency, system power-balance requirement, and the available capacity of the fuel cell under normal, derated, and outage states.

The equipment capacities in Table 3 are configured to match the power scale of the representative test system rather than the rated capacities of specific commercial units. In particular, the thermal generation source is modeled as an equivalent aggregated conventional generation unit. Its maximum output is set to 1500 kW, corresponding to approximately 60% of the peak load of the representative case. This setting allows the thermal source to provide sufficient dispatchable support while preventing it from independently covering the system peak demand. The hydrogen storage capacity is set to 2000 kWh on an HHV basis, corresponding to approximately 50.8 kg H_2, which is consistent with the approximately 50 kg H_2 storage scale reported in [41].

Consequently, renewable generation, ESS, HES, demand response, and external grid interaction are required to participate jointly in power balancing. The capacities of the ESS, EL, and hydrogen storage tank are likewise selected in coordination with the source–load scale to maintain feasible operation while preserving the need for multi-resource coordination.

The five representative joint WT–PV scenarios obtained after scenario reduction are shown in Figure 3. Each scenario consists of the corresponding WT and PV power profiles and represents a distinct joint renewable-generation pattern.

The seasonal composition of the samples assigned to each representative scenario is shown in Figure 4. The five scenarios are not predefined according to individual seasons; instead, each scenario contains samples from different seasons with different occurrence proportions.

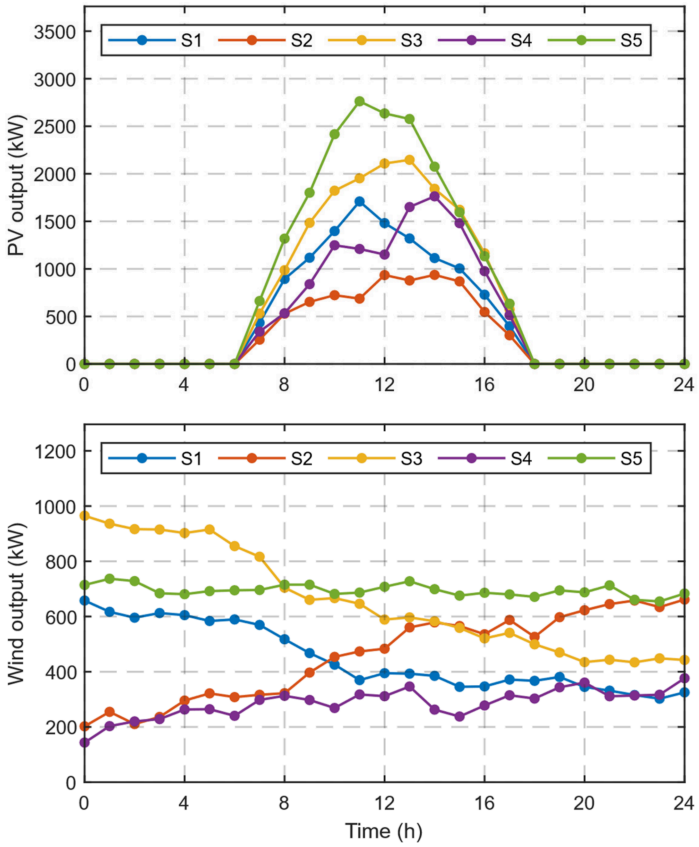


Figure 3. Five representative joint WT–PV scenarios.

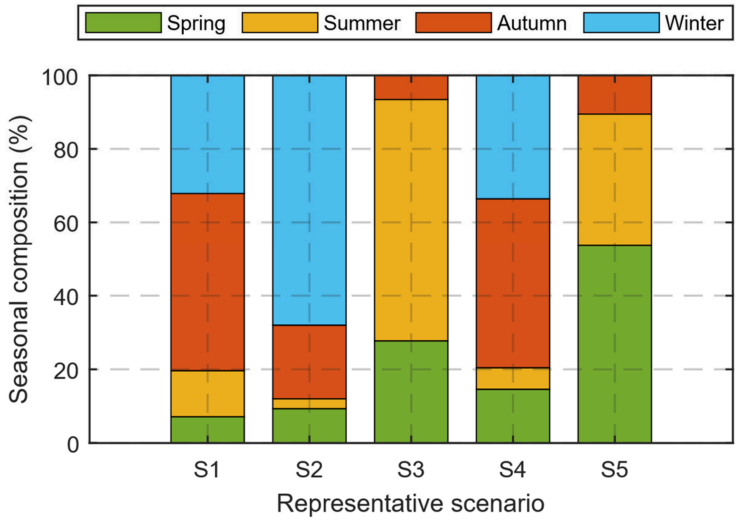


Figure 4. Typical scenarios of photovoltaic power output. Seasonal composition of the five representative joint WT–PV scenarios.

The five clustered scenarios are retained in the day-ahead stochastic optimization model, with each scenario representing a distinct joint WT–PV power pattern. Therefore, the stochastic scheduling results are obtained by considering the complete reduced scenario set rather than a single renewable-power scenario. To further illustrate the detailed source–load–storage coordination mechanism under a specific realization of renewable generation, Scenario 5 is selected for the subsequent 24 h power-balance analysis. Scenario 5 exhibits representative intra-day renewable-power variations and contains both periods of relatively high renewable generation and periods of tighter power supply, al-

lowing the charging/discharging behavior of the ESS, EL operation, fuel-cell generation, demand response, and grid interaction to be clearly demonstrated. The selection of Scenario 5 is thus intended for detailed operational illustration and does not imply that it corresponds to a specific season or that the other four scenarios are excluded from the stochastic optimization.

3.2. Source–Load–Storage Coordinated Operation Analysis Under Hydrogen Energy Equipment Failure Risk

As discussed in Section 3.1, all five reduced WT–PV scenarios are incorporated into the stochastic optimization. Scenario 5 is further selected as an illustrative case to examine the detailed 24 h source–load–storage coordination process. Figure 5 presents the resulting electrical power and energy balance under Scenario 5. Overall, the system satisfies the load demand through the coordinated operation of thermal power units, WT and PV generation, HFCs, ESS discharge, and electricity purchasing, while surplus electricity is accommodated through ELs, ESS charging, demand response, and electricity selling.

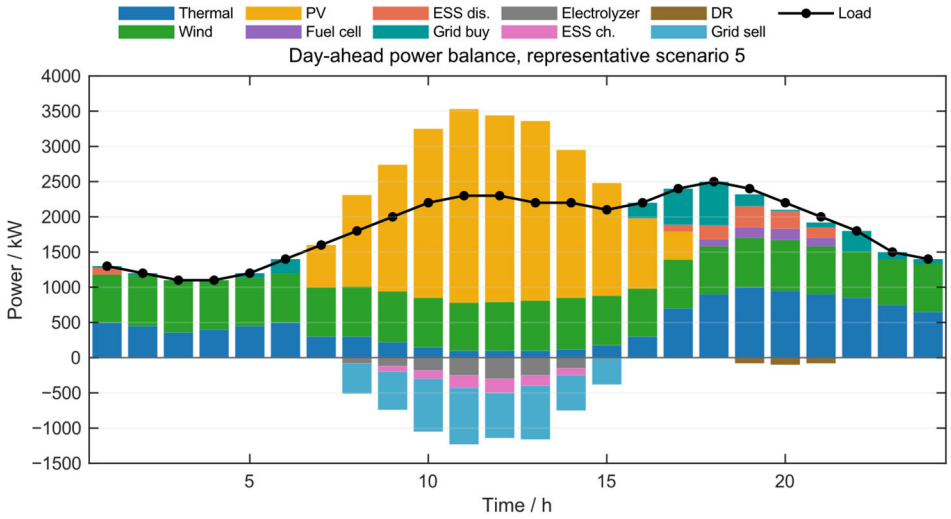


Figure 5. Day-ahead electrical power and energy balance under typical scenario 5.

During 0:00–6:00, the system is in a low-load period, and photovoltaic output is zero. The system mainly relies on thermal power and wind power for supply, with electricity purchased from the external grid to supplement the remaining demand in some periods. During 7:00–16:00, renewable energy output is high, and photovoltaic output increases rapidly and reaches its peak at noon. At this time, surplus renewable electricity is mainly balanced through electricity selling to the external grid, while ESS charging and EL operation are activated in some periods to store electrical energy or convert it into hydrogen, thereby improving renewable energy accommodation. During this period, the thermal power output is basically maintained at a relatively low level, indicating that renewable energy forms an obvious substitution effect on conventional units. During 17:00–21:00, the system enters the evening peak-load period, with photovoltaic output decreasing while the load remains at a high level. The system uses increased thermal power output, ESS discharge, HFC output, electricity purchasing from the external grid, and demand response for coordinated peak-load support. During 18:00–20:00, the system mobilizes flexible resources, such as ESS discharge, fuel cells, grid interaction, and demand response, to participate in power supply, thereby sharing the peak-regulation burden among multiple flexibility resources and improving the power supply flexibility and peak-load support capability of the system. During 22:00–24:00, the load gradually decreases, the output of energy storage and fuel cells is reduced, and the system again mainly relies

on thermal power, wind power, and external grid purchases for supply, while maintaining overall power and energy balance.

This case indicates that, during the peak period of wind and photovoltaic output, surplus renewable electricity is accommodated through grid export, ESS charging, and EL operation. During the load peak period, peak shaving and valley filling are realized through the coordinated operation of thermal generation, energy storage discharge, fuel cells, grid interaction, and demand response, thereby improving the operational flexibility of the system.

Figure 6 shows the operating results of the EL and HFC, respectively. It can be seen from the figure that the fault state of hydrogen energy equipment constrains the original dispatch plan by changing its available capacity upper limit. When the planned power of the equipment is lower than the available capacity, the fault state does not directly change the equipment output; when the planned power exceeds the available capacity, the actual output of the equipment is limited, forming a corresponding power imbalance in the system.

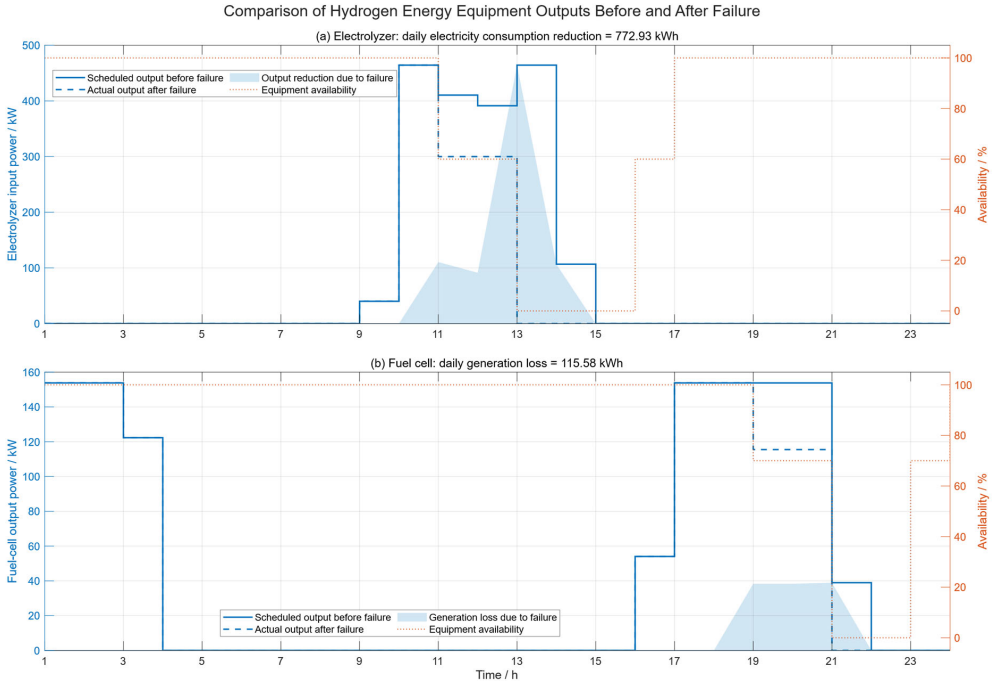


Figure 6. Output responses of the EL and HFC under non-simultaneous equipment failures.

Under the fault-free baseline, the EL is scheduled to operate mainly during 9:00–15:00 to absorb surplus renewable electricity. In practical operation, EL faults may originate from abnormal stack operating conditions, insufficient water supply, gas-pressure deviations, cooling-system faults, power-electronic failures, or other auxiliary-system abnormalities. Mild faults may trigger protective power limitation and reduce the maximum admissible operating current or power, corresponding to the derated state considered in this study, whereas severe faults may activate protection or shutdown procedures, corresponding to the outage state. Therefore, the influence of these physical faults is represented in the scheduling model through a state-dependent available capacity coefficient. However, under the fault scenario, the EL enters a derating state during 11:00–13:00, and its available capacity decreases to approximately 300 kW. As a result, its actual operating power is constrained by the reduced capacity limit and becomes lower than the planned power in the fault-free case. During 13:00–16:00, the EL further enters the outage state, and its available capacity decreases to 0 kW, making hydrogen production unavailable. The resulting daily reduction in EL electricity consumption is approximately 772.93 kWh. The

derating and outage reduce the EL's ability to absorb surplus electricity, resulting in lower hydrogen production and a decrease in the hydrogen storage level. The surplus electricity that cannot be absorbed by the EL is then rebalanced through ESS charging, electricity selling to the external grid, or adjustment of renewable energy accommodation.

During 0:00–3:00 and 15:00–19:00, the planned power of the HFC does not exceed its available capacity; therefore, the dispatch results before and after the fault are basically consistent. Around 19:00–21:00, the fuel cell is in the derating state, and its available capacity decreases from approximately 160 kW under the normal condition to approximately 115 kW. Its actual output is correspondingly limited. Around 21:00–23:00, the fuel cell enters the outage state and cannot provide electricity according to the original plan. The resulting daily generation loss is approximately 115.58 kWh. Among these periods, a relatively obvious power supply shortage occurs during 19:00–20:00. This shortage needs to be jointly compensated by flexible resources such as increased thermal power generation, ESS discharge, external electricity purchasing, or demand response. After 23:00, the available capacity of the equipment gradually recovers. Since the planned output at this time is lower than the restored capacity upper limit, the fault state no longer constrains its actual output.

Therefore, the system-level propagation mechanism of an EL fault can be summarized as follows: component or auxiliary-system abnormalities reduce the available EL capacity, which limits electrical power absorption and hydrogen production; the resulting reduction in hydrogen storage modifies the subsequent hydrogen-to-electricity capability, while the instantaneous surplus electrical power must be redistributed among the ESS, external grid, demand response, and renewable-power adjustment.

Figure 7 shows the power deviation caused by hydrogen energy equipment failures, the system compensation power, and the variation in hydrogen storage before and after the failures. The bar chart represents the compensation power provided by renewable energy output adjustment, distribution network power adjustment, and demand response. The black dashed line denotes the power deficit caused by hydrogen energy equipment failures, while the blue solid line and red dashed line represent the hydrogen storage under normal and fault conditions, respectively.

During 0:00–8:00, no failure occurred in the hydrogen energy equipment that affected its scheduled output. Therefore, the net power gap was approximately zero, and the hydrogen storage profiles before and after the failure remained consistent. After 9:00, the available capacity of the EL decreased, and its actual power consumption became lower than the scheduled value under normal conditions, resulting in surplus electrical power in the system. To maintain power and energy balance, the system correspondingly reduced the actual renewable energy consumption. The largest adjustment occurred around 12:00, which generally corresponded to the maximum reduction in EL power consumption in this period. This indicates that the EL failure weakened the system's capability to absorb surplus renewable energy and convert it into hydrogen energy.

Affected by the reduction in EL hydrogen production power, the hydrogen storage under the fault condition was significantly lower than that under the normal condition after 9:00. Under normal conditions, hydrogen storage continued to increase during periods with high renewable energy output and reached its peak during 13:00–14:00. Under the fault condition, due to the reduced hydrogen production, the hydrogen storage only increased to a lower level and remained relatively stable for a period before decreasing as hydrogen was subsequently consumed by the fuel cell. This indicates that the EL failure not only affects the electrical power and energy balance in the current period but also has an intertemporal impact on subsequent fuel-cell operation through the hydrogen storage state.

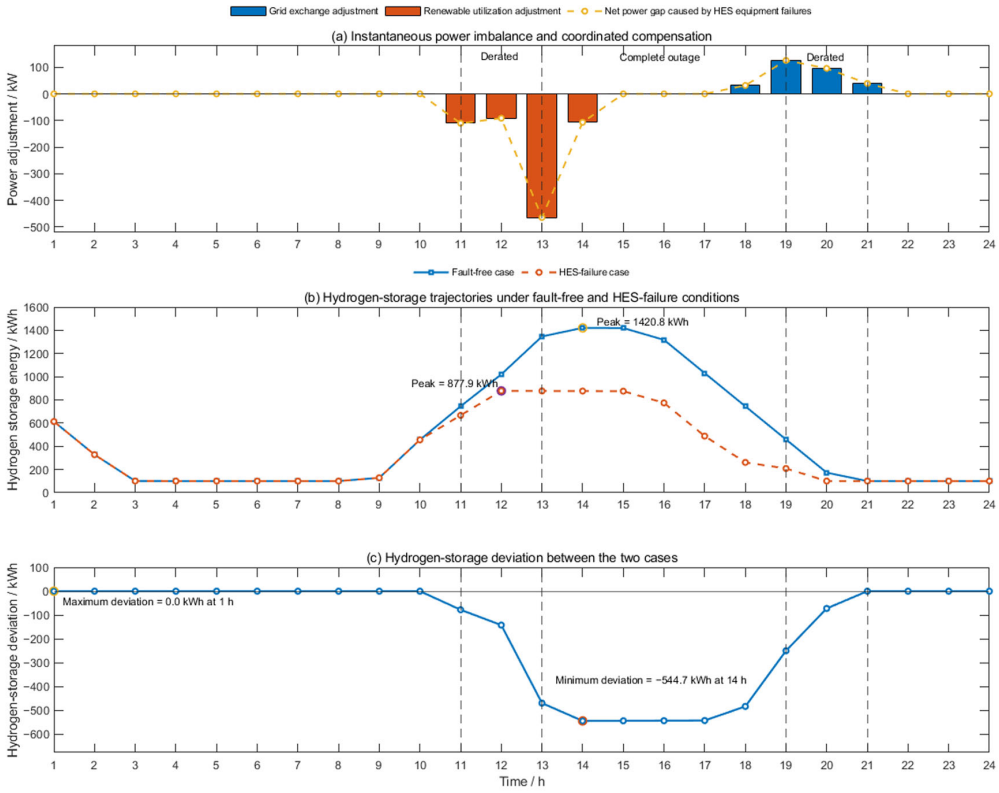


Figure 7. System-level response under non-simultaneous failures of the EL and HFC.

During 17:00–20:00, the actual power generation of the HFC was lower than the original scheduled value. As a result, the system changed from having surplus electrical power to experiencing a power supply shortage. The positive net power gap was mainly compensated for by increasing power exchange with the external grid, with the largest compensation occurring around 18:00. The grid exchange adjustment was generally consistent with the positive net power gap caused by the hydrogen energy equipment failure, indicating that grid interaction can effectively compensate for the power supply shortage caused by HFC failures.

Figure 7c further quantifies the deviation in hydrogen storage between the fault and fault-free cases. The deviation increases after the EL failure and reaches approximately −544.7 kWh at 14:00, indicating that the reduction in hydrogen production causes a pronounced cumulative impact on the hydrogen storage state over subsequent periods.

The above analysis considers temporally differentiated availability disturbances of the EL and fuel cell. To further examine the system response under a more severe equipment-availability condition, an additional stress-test case is introduced in which the two hydrogen energy devices experience simultaneous derating and outage periods.

As shown in Figure 8, simultaneous failures impose a more restrictive constraint on the electricity–hydrogen subsystem than the base failure case. During the overlapping derating and outage periods, the available operating capacities of both the EL and fuel cell decrease simultaneously. Consequently, the EL loses part of its capability to absorb surplus renewable electricity and convert it into hydrogen, while the fuel cell simultaneously loses part of its capability to provide electrical power from stored hydrogen. The accumulated unavailable energy reaches approximately 772.93 kWh for the EL and 399.95 kWh for the fuel cell, respectively.

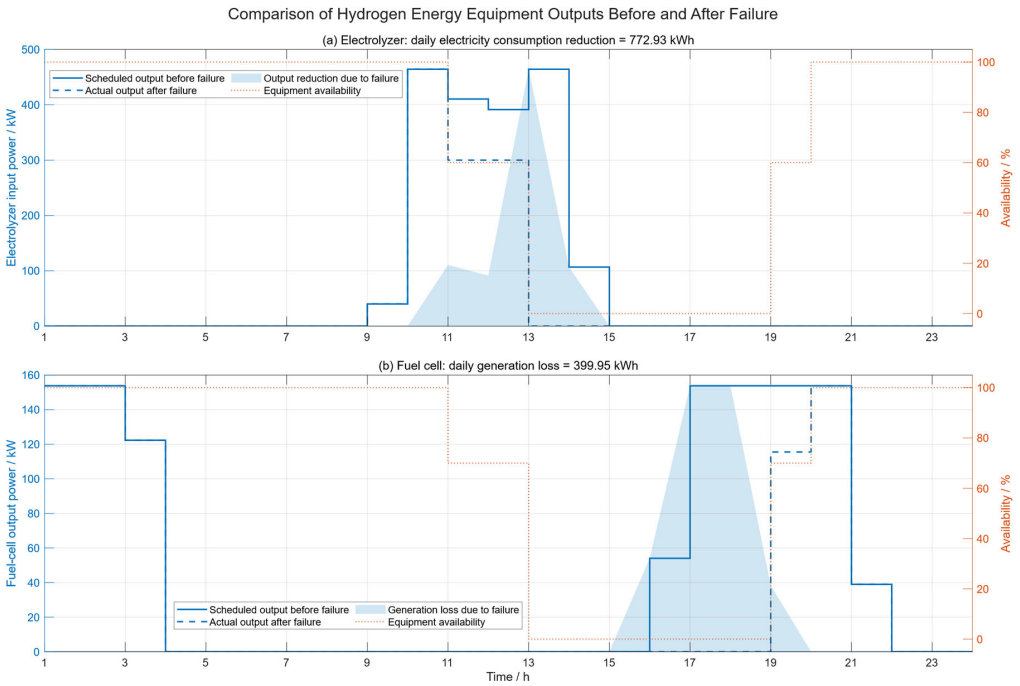


Figure 8. Output responses of the EL and HFC under simultaneous equipment failures.

This simultaneous reduction in both electricity-to-hydrogen and hydrogen-to-electricity conversion capability substantially weakens the bidirectional regulation flexibility of the HES. Therefore, a larger balancing burden must be transferred to the ESS, thermal generation, demand response, and grid interaction. The results demonstrate that the proposed framework can explicitly represent overlapping equipment-availability disturbances and adapt the coordinated dispatch accordingly under more severe HES-failure conditions.

The preceding results illustrate the direct impact of simultaneous failures on the available operating capacities of the EL and fuel cell. To further investigate how these equipment-level disturbances propagate to the system level, Figure 9 presents the resulting power imbalance, coordinated compensation by flexible resources, and the corresponding evolution of the hydrogen storage state.

As shown in Figure 9a, during the early stage of the simultaneous-failure interval, the reduction in EL power consumption is the dominant disturbance. Because the EL can no longer absorb electricity according to the original schedule, an electrical surplus emerges, as indicated by the negative net power gap. The system primarily compensates for this surplus by reducing renewable energy utilization. The largest adjustment occurs around 12:00, coinciding with the period in which the EL experiences the greatest loss of scheduled power consumption.

As the operating horizon progresses, the dominant effect shifts from reduced EL consumption to insufficient fuel-cell generation. When the fuel cell is expected to provide power but remains derated or unavailable, the net power gap changes from surplus to shortage. During approximately 15:00–18:00, the positive power deficit is mainly compensated through grid exchange adjustment. This transition demonstrates that simultaneous HES failures can produce bidirectional disturbances: EL failure may create surplus electricity by reducing controllable consumption, whereas fuel-cell failure may subsequently create a supply deficit by reducing dispatchable generation.

Figure 9b further shows that the simultaneous failures have a pronounced intertemporal impact on the hydrogen storage state. Under the fault-free condition, the hydrogen inventory increases rapidly during the high-renewable period because surplus electricity is converted into hydrogen through the EL. Under simultaneous failures, however, the

reduction and subsequent loss of EL availability significantly suppress hydrogen production. Consequently, the hydrogen storage level remains substantially below the fault-free trajectory during the midday period and exhibits an extended plateau during the complete-outage interval.

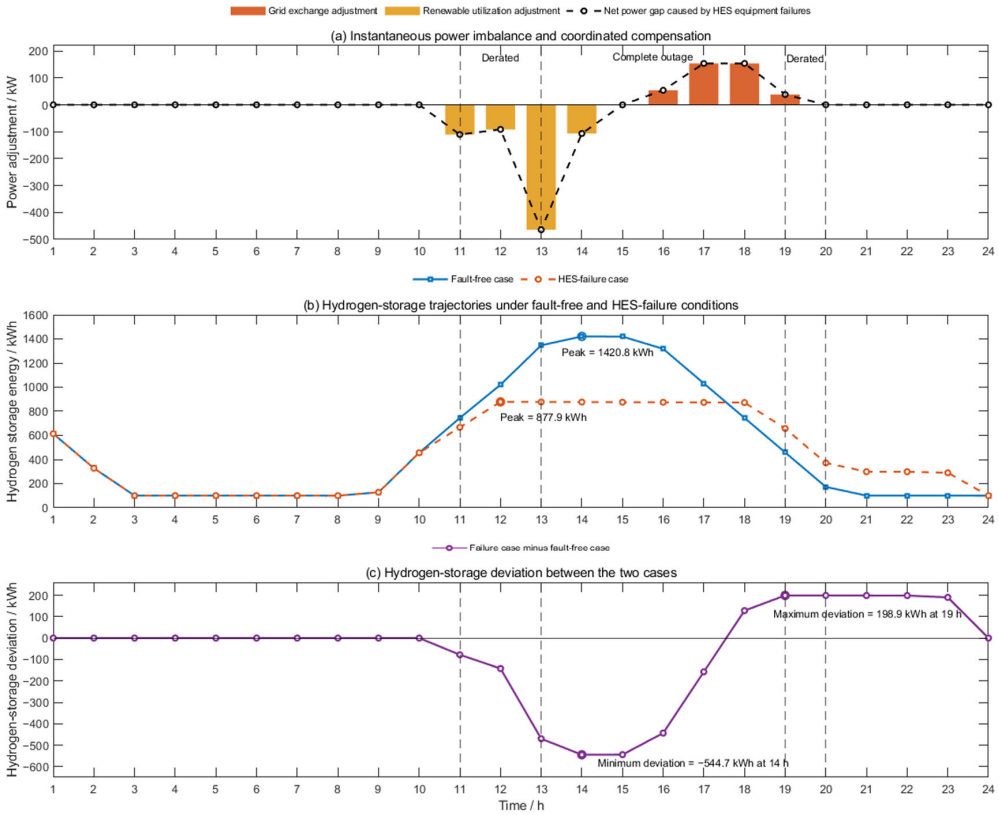


Figure 9. System-level response under simultaneous EL and fuel-cell failures.

Figure 9c quantitatively shows the resulting deviation in hydrogen storage. The deviation reaches approximately −544.7 kWh at 14:00 and subsequently becomes positive, reaching about 198.9 kWh at 19:00, reflecting the combined effects of reduced hydrogen production by the EL and restricted hydrogen consumption by the fuel cell.

An additional feature can be observed during the evening period. Although the hydrogen inventory is initially lower under the failure condition because of reduced hydrogen production, it subsequently decreases more slowly than in the fault-free case. This occurs because the simultaneous derating or outage of the fuel cell also restricts hydrogen consumption. As a result, part of the stored hydrogen cannot be converted back into electricity according to the original dispatch plan, causing the fault-case hydrogen inventory to exceed the fault-free trajectory during the later operating periods.

Overall, Figures 8 and 9 demonstrate that simultaneous EL and fuel-cell failures introduce both instantaneous and intertemporal disturbances into the electricity–hydrogen coupled system. At the electrical level, the disturbance changes from surplus power caused by reduced EL consumption to supply shortage caused by insufficient fuel-cell generation, requiring different flexible resources to participate in coordinated compensation. At the energy level, reduced hydrogen production and restricted subsequent hydrogen consumption jointly reshape the hydrogen storage trajectory. These results confirm that simultaneous HES failures cannot be represented solely as an instantaneous power-capacity reduction; instead, their effects propagate across operating periods through the hydrogen storage state.

Despite these more severe overlapping disturbances, the coordinated scheduling framework dynamically reallocates the balancing task among renewable energy adjustment, grid interaction, and other flexible resources, demonstrating its ability to accommodate simultaneous hydrogen energy equipment failures.

3.3. Analysis of the Low-Carbon Economic Performance of the Dynamic Carbon Quota Mechanism

To clearly distinguish the effects of different components, five schemes are designed for comparative analysis. Scheme A represents the baseline case without hydrogen energy equipment or fault modeling, while MPC and dynamic carbon quota allocation are adopted. Scheme B introduces hydrogen energy equipment based on Scheme A, but equipment faults are not considered. Scheme C considers hydrogen energy equipment and fault modeling, but MPC is not adopted. Scheme D considers hydrogen energy equipment, fault modeling, and MPC, but adopts a static carbon quota mechanism. Scheme E is the proposed scheme, in which hydrogen energy equipment, fault modeling, MPC, and the dynamic carbon quota mechanism are all considered. RMSE is used to evaluate the residual power tracking deviation after intra-day correction.

The total system operating cost reported in Table 4 is calculated based on the actual economic operating cost terms defined in Section 2.4.3. Specifically, it includes the start-up and shutdown costs of the thermal generation unit, reserve costs, thermal generation operating costs, demand response compensation costs, external grid interaction costs, and carbon-trading costs. The scenario-dependent cost terms are weighted by their corresponding scenario probabilities, and all operating cost components are aggregated over the 24 h scheduling horizon using the same calculation method for all schemes. The task tracking penalty term in Equation (61) is introduced only for optimization purposes and is not included in the total system operating cost reported in Table 4.

Table 4. Economic and low-carbon performance comparison of different operation schemes.

Indicator	Total System Operating Cost/$	Actual Carbon Emissions/t	RMSE/kW
Scheme A	19,012	17.3	85
Scheme B	16,288	16	60
Scheme C	17,519	16.4	188
Scheme D	16,827	17.1	47
Scheme E	15,323	15.6	9.39

As shown in Table 4, the five schemes present different economic and low-carbon performances under different system configurations. Scheme A, which does not consider hydrogen energy equipment, has the highest total system operating cost of $19,012, indicating that the absence of hydrogen energy storage and conversion limits the system's ability to absorb surplus renewable energy. After introducing hydrogen energy equipment in Scheme B, the total system operating cost decreases to $16,288 and the actual carbon emissions decrease from 17.3 t to 16 t. This demonstrates that hydrogen energy equipment can improve renewable energy accommodation and reduce both operating cost and carbon emissions.

Compared with Scheme C, which does not adopt MPC, Scheme E significantly improves system performance. The total system operating cost decreases from $17,519 to $15,323, corresponding to a reduction of $2196 or 12.53%. And the actual carbon emissions decrease from 16.4 t to 15.6 t. Meanwhile, the RMSE decreases from 188 kW to 9.39 kW, indicating that MPC can effectively improve the tracking accuracy and operational stability of the system under fault conditions.

Furthermore, by comparing Scheme D and Scheme E, the effect of the dynamic carbon quota mechanism can be observed. Scheme D adopts a static carbon quota mechanism,

while Scheme E adopts a dynamic carbon quota mechanism under the same conditions of hydrogen energy equipment, fault modeling, and MPC. The total system operating cost decreases from \$16,827 to \$15,323, with a reduction of \$1504 or 8.94%. The actual carbon emissions decrease from 17.1 t to 15.6 t, representing a reduction of 1.5 t or 8.77%. These results show that the dynamic carbon quota mechanism can effectively reduce carbon trading cost and carbon emissions while improving the overall economy of the system.

Overall, Scheme E achieves the lowest total system operating cost, the lowest actual carbon emissions, and the smallest RMSE among all schemes. This verifies that the coordinated strategy integrating hydrogen energy equipment, fault modeling, MPC, and dynamic carbon quota allocation can achieve better economic performance, low-carbon operation, and power tracking accuracy.

As shown in Figure 10, to evaluate the sensitivity of the dynamic carbon quota mechanism, the load-level coefficient was varied from 0.10 to 0.40 around the base-case value of 0.25. Under low-load conditions, the total operating cost increases slightly while carbon emissions decrease marginally. This is mainly because the system has relatively sufficient supply flexibility, and the redistribution of the fixed carbon budget slightly tightens the carbon constraint in some periods. In contrast, under high-load conditions, a larger coefficient allocates more carbon quota to load-intensive periods, thereby relaxing the carbon constraint during periods with greater supply pressure. Consequently, the use of costly regulation resources is reduced, leading to a lower operating cost but moderately higher carbon emissions.

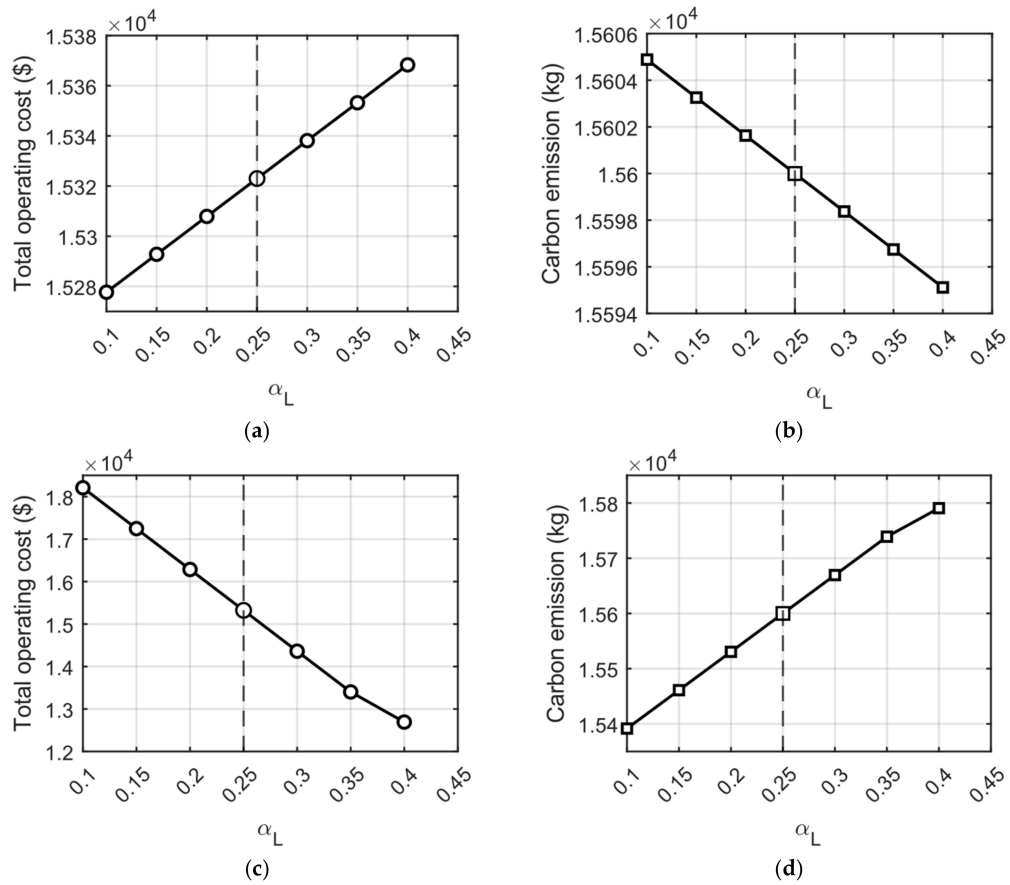


Figure 10. Sensitivity of total operating cost and carbon emissions to the load-level influence coefficient: (**a**,**b**) low-load conditions; (**c**,**d**) high-load conditions.

As shown in Figure 11, the renewable energy penetration coefficient was varied from 0.10 to 0.50 around the base-case value of 0.30. As the coefficient increases, the total oper-

ating cost increases while carbon emissions decrease, with both changes becoming more pronounced beyond the base-case value. According to Equation (26), a larger coefficient strengthens the reduction in the dynamic quota weight associated with high renewable energy penetration, thereby assigning relatively tighter carbon quotas to periods with greater renewable availability. This encourages greater utilization of renewable energy and other flexible resources instead of thermal generation, resulting in lower carbon emissions but higher operating costs. The stronger variation beyond 0.30 indicates that further tightening of the carbon allocation increasingly relies on costly flexibility resources, leading to a growing marginal cost of emission reduction.

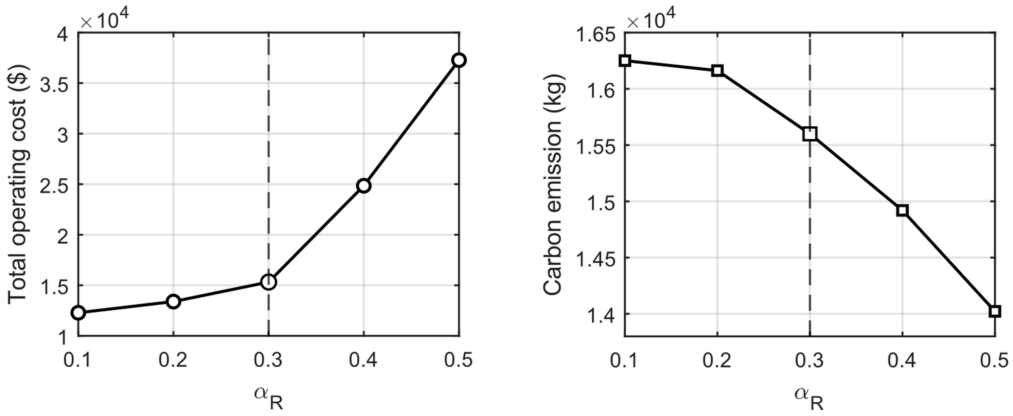


Figure 11. Sensitivity of total operating cost (**a**) and carbon emissions (**b**) to the renewable energy penetration coefficient.

As shown in Figure 12, the HES availability coefficient was varied from 0.10 to 0.50 around the base-case value of 0.20. As the coefficient increases, the total operating cost decreases steadily, while carbon emissions increase moderately. This is because a larger coefficient allocates relatively more carbon quota to periods with higher HES unavailability risk, thereby relaxing the carbon constraint when low-carbon flexibility is reduced by equipment derating or outages. Consequently, the system relies more on conventional generation to maintain power and energy balance, reducing the need for costly regulation measures but leading to higher carbon emissions. These results reveal a clear trade-off between operating economy and emission reduction under HES availability uncertainty.

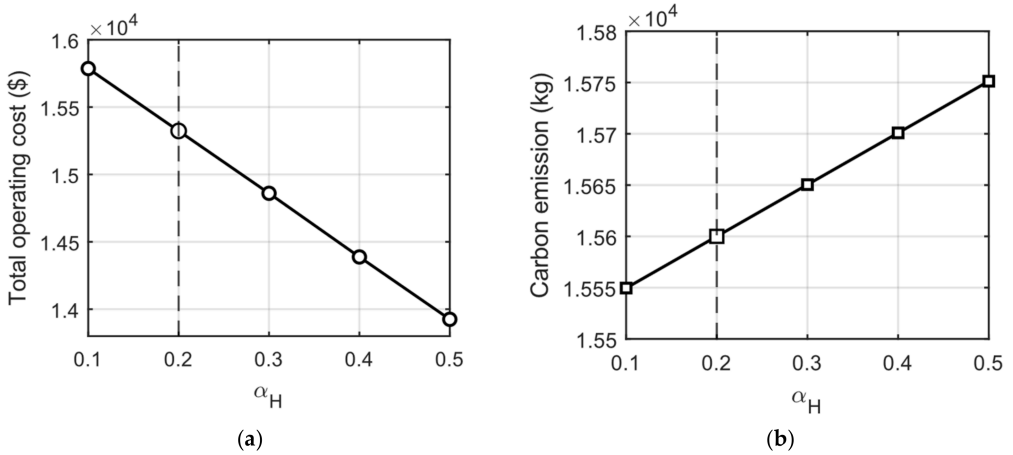


Figure 12. Sensitivity of total operating cost (**a**) and carbon emissions (**b**) to the HES availability coefficient.

3.4. Analysis of Intra-Day Rolling Optimization and Feedback Correction Considering Uncertainty in the Decomposed Schedule

Figure 13 presents the intra-day incremental regulation of multiple flexible resources relative to the day-ahead dispatch schedule shown in Figure 5. The power deviation before correction exhibits pronounced fluctuations, particularly during the periods of high renewable energy output and rapid load variation. During 0:00–6:00, relatively small deviations are mainly compensated by thermal generation, ESS, and grid interaction adjustments. During 7:00–16:00, when renewable generation is relatively high, ESS and grid interaction provide the major balancing capability, while renewable-power adjustment and EL regulation provide additional flexibility in periods with surplus power. The limited thermal adjustment during this period is consistent with the relatively low thermal-unit output in the day-ahead schedule.

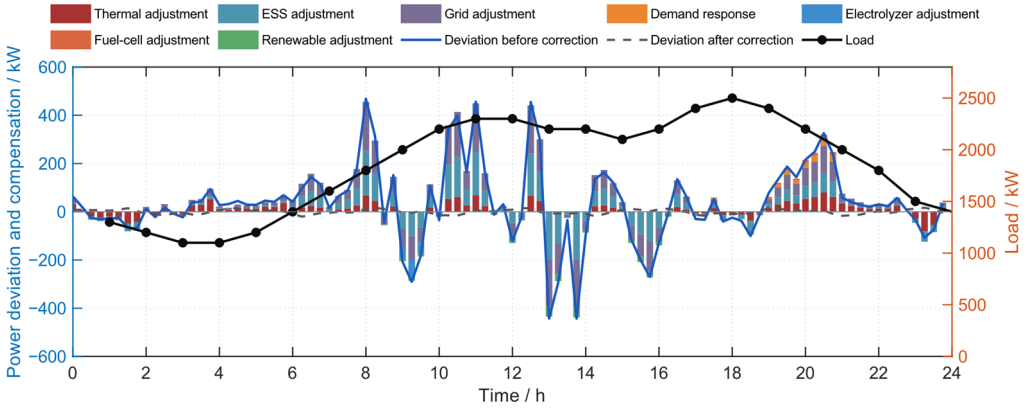


Figure 13. Power deviation correction and multi-resource compensation under intra-day MPC rolling optimization.

During the evening peak period of 17:00–21:00, positive regulation requirements increase as the load remains high and photovoltaic generation decreases. Thermal units, ESS, grid interaction, demand response, and fuel cells jointly provide upward regulation, which is consistent with the coordinated peak-load support strategy shown in Figure 5. After 21:00, as the load gradually declines, the required regulation decreases and is mainly provided by thermal units, ESS, and grid interaction. After MPC-based rolling correction, the residual power deviation remains close to zero, with an RMSE of 9.39 kW, demonstrating the effectiveness of the proposed intra-day feedback-correction strategy.

3.5. Sensitivity Analysis of Hydrogen Equipment Failure Parameters

To evaluate the influence of hydrogen equipment reliability parameters on the scheduling results, a sensitivity analysis is conducted by introducing a failure-rate multiplier κ. Specifically, all transition rates of the Markov model are scaled as $\lambda'_{ij} = \kappa\lambda_{ij}$, where $\kappa = 1$ represents the baseline condition.

As shown in Figure 14, increasing κ gradually reduces the expected available capacities of ELs and HFCs, demonstrating the impact of intensified failure risks on hydrogen equipment availability. The vertical dashed lines in Figure 14b–d indicate the values of κ adopted in this study. Meanwhile, the relative operating cost increases with κ, indicating that additional flexibility resources and grid power are required to compensate for the reduced hydrogen storage capability.

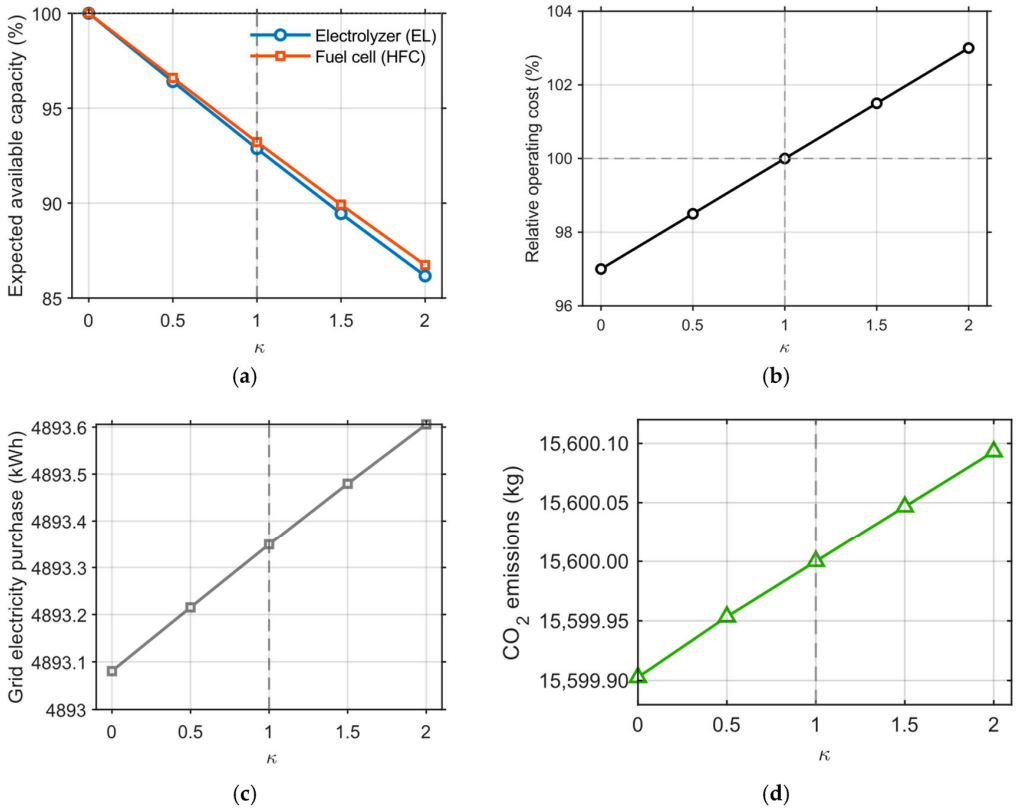


Figure 14. Sensitivity analysis of hydrogen equipment failure parameters: (**a**) expected available capacity of hydrogen equipment; (**b**) relative operating cost; (**c**) grid electricity purchase; (**d**) carbon emissions.

The sensitivity results demonstrate that although hydrogen equipment failures negatively affect system economy and flexibility, the proposed multi-time-scale optimization framework maintains stable scheduling performance under different reliability conditions.

3.6. Robustness and General Applicability Under Alternative Operating Conditions

To examine the robustness of the proposed framework under higher renewable energy penetration, the installed WT and PV capacities were uniformly scaled to 1.00, 1.25, and 1.50 times their base-case values, corresponding to renewable energy penetration levels of 65.79%, 82.24%, and 98.68%, respectively. The remaining model parameters and scheduling settings were kept unchanged. The corresponding results are summarized in Table 5.

Table 5. Performance of the proposed method under different renewable energy penetration levels.

RE Penetration	Total System Operating Cost/$	Actual Carbon Emissions/t	RE Accommodation
65.79%	15,323	15.6	98.47%
82.24%	14,631	14.9	91.02%
98.68%	13,864	13.5	82.86%

As the renewable energy penetration increases from 65.79% to 98.68%, the total system operating cost decreases from $15,323 to $13,864, corresponding to a reduction of approximately 9.52%. Meanwhile, the actual carbon emissions decrease from 15.6 t to 13.5 t, representing reductions of approximately 13.46%. These results indicate that the proposed coordinated scheduling framework can effectively exploit the economic and low-carbon benefits of increased renewable generation.

However, the renewable energy accommodation rate decreases from 98.47% to 82.86% as the penetration level increases. This result indicates that, although a higher renewable share reduces conventional generation and carbon emissions, the existing flexibility resources gradually become insufficient to absorb all available renewable generation. Therefore, the marginal accommodation capability of the system becomes more constrained at extremely high renewable penetration levels.

The sensitivity to load-profile variation was further investigated using three representative load patterns while keeping the total daily electricity demand unchanged. The baseline profile corresponds to the original case. For the enhanced evening peak profile, the load during 11:00–15:00 was reduced by 10%, while the load during 18:00–22:00 was increased by 15%, followed by normalization to preserve the total daily electricity consumption. The flattened profile was constructed by combining 70% of the baseline profile with 30% of its daily average value, also preserving the same total daily energy demand.

Table 6 shows that the proposed method maintains comparable economic and low-carbon performance under all three load profiles. Relative to the baseline case, the total operating cost changes from \$15,323 to \$15,030 under the enhanced evening peak profile and to \$14,922 under the flattened profile. The corresponding carbon emissions remain within a narrow range of 15.4–15.6 t. The relatively limited variation in these performance indicators indicate that the effectiveness of the proposed framework is not strongly dependent on a specific temporal load pattern. Among the tested profiles, the flattened load case yields the lowest operating cost and carbon emissions, because reduced peak–valley variation alleviates the demand for high-cost peak-regulation resources. Nevertheless, all three cases remain economically feasible and preserve the low-carbon scheduling characteristics of the proposed strategy.

Table 6. Performance of the proposed method under different load profiles.

Load Profile	Total System Operating Cost/\$	Actual Carbon Emissions/t
Baseline load profile	15,323	15.6
Enhanced evening peak profile	15,030	15.5
Flattened load profile	14,922	15.4

Figure 15 shows the effects of carbon trading price variations on the dispatching economy and carbon emission level of the system. The red dashed line marks the carbon trading price of 60 \$/t adopted in this study. It can be observed that, as the carbon trading price increases from 10 \$/t to 150 \$/t, the actual carbon emissions of the system generally show a decreasing trend and tend to stabilize in the high carbon price range. This indicates that the carbon trading mechanism can effectively guide the system to reduce carbon emissions. However, when emission reduction reaches the boundary imposed by equipment operating constraints or dispatching capability, further increases in the carbon price have a limited effect on additional emission reduction.

In terms of the variation in the total system cost, the total cost first increases and then decreases as the carbon price rises. When the carbon price is relatively low, the system lacks sufficient incentives for emission reduction, and the actual carbon emissions exceed the carbon quota, resulting in additional carbon trading costs. Therefore, the total system cost gradually increases. When the carbon price rises to approximately 60 \$/t, the total system cost reaches a relatively high level, while the actual carbon emissions approach the carbon quota level. Subsequently, as the carbon price continues to increase, the system reduces carbon emissions through optimized dispatching, thereby decreasing the carbon trading penalty cost and gradually reducing the total system cost.

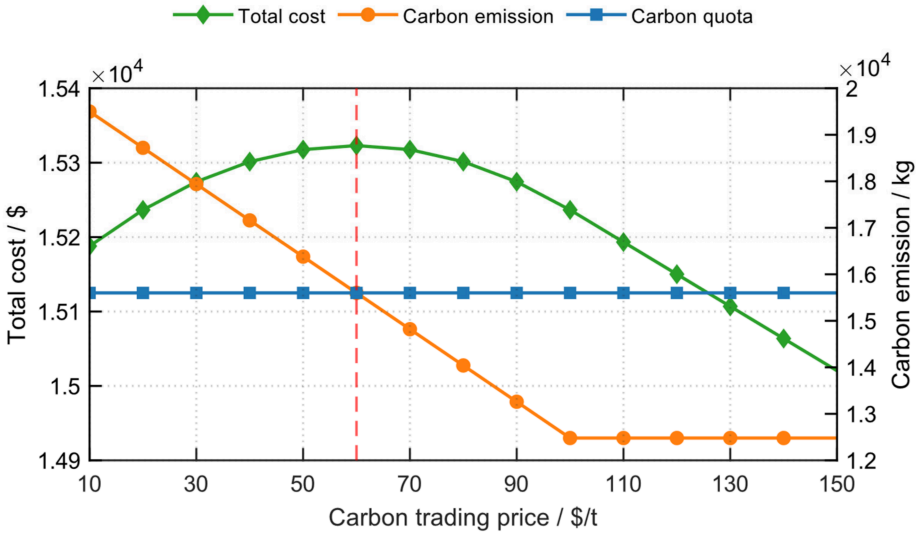


Figure 15. Sensitivity analysis of carbon trading price on total cost, carbon emissions, and carbon quota.

3.7. Computational Performance and Convergence Analysis

All optimization models were implemented in MATLAB R2023b using the YALMIP toolbox. The resulting mixed-integer linear programming (MILP) problems were solved using Gurobi 10.0.1 with its default parameter settings. All simulations were performed on a computer equipped with an Intel Core i7-12700H CPU (2.30 GHz) and 16 GB RAM, running Windows 11 64-bit.

To further evaluate the computational scalability with respect to the number of retained stochastic scenarios, additional tests were conducted by varying the number of reduced scenarios K from 3 to 20. Table 7 reports the corresponding scenario-reduction and day-ahead optimization times. As K increases from 3 to 20, the scenario-reduction time increases moderately from 1.54 s to 2.26 s, whereas the day-ahead optimization time increases from 2.24 s to 14.20 s. The results show that the computational burden of scenario reduction remains relatively limited, while the solution time of the day-ahead stochastic optimization increases with the number of retained scenarios because of the corresponding growth in scenario-dependent decision variables and constraints. Nevertheless, all tested cases were solved within 15 s, indicating acceptable computational scalability for the range of scenario sizes considered in this study.

Table 7. Computational-time performance under different numbers of reserved scenarios.

Number of Retained Scenarios K	Scenario-Reduction Time (s)	Day-Ahead Optimization Time (s)
3	1.54	2.24
5	1.56	3.60
7	1.68	4.86
10	1.89	6.84
20	2.26	14.20

The computational efficiency of the proposed rolling optimization framework was also evaluated by recording the solution time of each optimization instance. The average solution time was 0.274 s, while the maximum solution time was 0.366 s. The total computational time for the complete rolling optimization process was 26.314 s. These results demonstrate that the proposed framework achieves sub-second solution times for

individual rolling optimization problems under the system scale and scenario settings considered in this study.

To further evaluate the closed-loop convergence characteristics of the proposed intra-day MPC strategy, the realized power-balance error and the evolution of the cumulative RMSE were analyzed, as shown in Figures 16 and 17. Figure 16 shows that the closed-loop power-balance error fluctuates around zero throughout the 24 h operating horizon without exhibiting persistent positive or negative drift. Although short-term deviations occur because of renewable-generation uncertainty, load fluctuations, and changes in hydrogen energy storage availability, the feedback-correction mechanism continuously compensates for these disturbances and prevents the accumulation of systematic power imbalance.

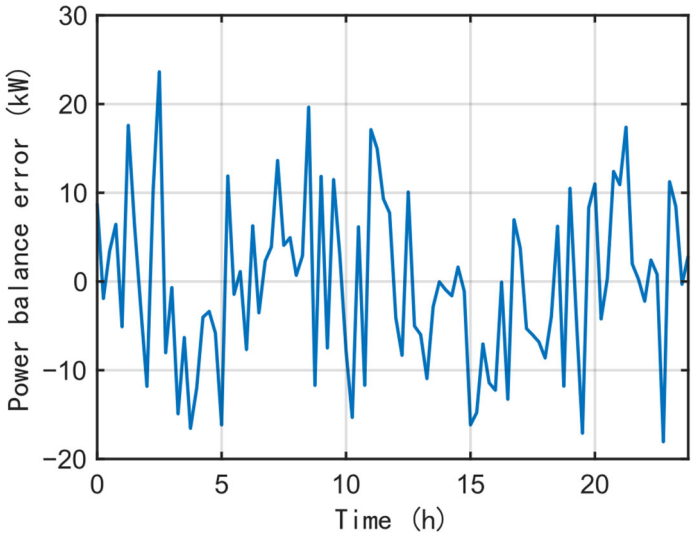


Figure 16. Closed-loop power-balance error under intra-day MPC rolling optimization.

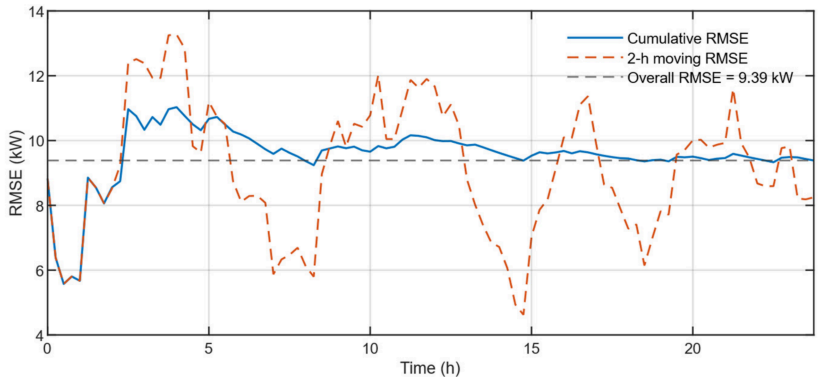


Figure 17. Evolution of cumulative RMSE during closed-loop MPC operation.

Figure 17 further presents the evolution of the cumulative RMSE during the rolling optimization process. Relatively large variations can be observed during the initial operating periods because the cumulative metric is sensitive to individual errors when only a limited number of observations are available. As additional MPC steps are implemented, the influence of individual short-term deviations gradually decreases, and the cumulative RMSE progressively stabilizes. At the end of the 24 h scheduling horizon, the closed-loop RMSE converges to approximately 9.39 kW. The absence of sustained growth or oscillatory divergence in the cumulative RMSE indicates that the proposed MPC-based feedback correction maintains stable closed-loop power-balancing performance over successive rolling periods.

4. Discussion

The results demonstrate that the proposed framework provides a coordinated approach for addressing renewable energy uncertainty, hydrogen energy storage (HES) availability risk, and carbon constraints across multiple scheduling horizons. Compared with studies that mainly investigate the flexibility benefits of hydrogen storage under normal operating conditions [6–13], the present results further show that HES availability has an important influence on system balancing. EL derating or outage reduces the absorption of surplus renewable electricity and lowers the hydrogen inventory, which may subsequently restrict fuel-cell power support. Therefore, HES failures can propagate from an instantaneous power imbalance to a cross-period energy imbalance. This finding indicates that equipment availability should be explicitly considered when evaluating the operational flexibility provided by hydrogen storage.

Previous low-carbon scheduling studies have shown that carbon trading and carbon-related constraints can reduce emissions and improve system economy [14–20]. The proposed method further couples carbon allowance allocation with load level, renewable energy penetration, and HES availability. Consequently, the carbon budget can be redistributed according to actual operating conditions without changing the total daily carbon constraint. The comparison with the static carbon allowance scheme shows that this mechanism can improve the coordination between economic operation and emission reduction. In addition, the carbon price sensitivity analysis indicates that emission reduction is ultimately limited by the available operational flexibility, because further increases in carbon price provide only limited benefits once system regulation capability approaches its boundary.

The proposed multi-time-scale framework also extends existing day-ahead/intra-day and MPC-based scheduling approaches [21–28]. In addition to correcting short-term power deviations, the intra-day MPC continuously tracks the remaining generation task and carbon budget issued by the upper scheduling layer. This helps prevent repeated short-term corrections from causing cumulative deviations from medium- and long-term energy and emission targets. From a practical perspective, the framework is compatible with the operation of energy-management systems: periodic energy and carbon targets can be decomposed into daily tasks, a 24 h baseline schedule can be generated using day-ahead forecasts, and intra-day decisions can then be updated using renewable output, load demand, storage states, and HES availability. Therefore, the method may be applicable to renewable-rich microgrids, integrated energy systems, and electricity–hydrogen coupled systems.

Several limitations should also be acknowledged. First, the results are based on a 30-day case study with a specific system configuration, and further validation is required under different renewable penetration levels, seasonal conditions, network structures, and carbon-market rules. Second, the HES reliability model uses three Markov states and assumes a memoryless transition process, while the transition parameters are based on representative operating characteristics and engineering assumptions. Future studies should calibrate these parameters using actual reliability and maintenance data. Third, more advanced probabilistic forecasting methods may be introduced to better characterize renewable-generation uncertainty. Finally, the computational scalability of the proposed stochastic-MPC framework should be further evaluated in larger multi-node systems. Future work will therefore focus on longer-term operational validation, data-driven HES reliability modeling, more realistic carbon-market mechanisms, and real-time implementation.

5. Conclusions

This study proposed a multi-time-scale power and energy balance optimization method for highly uncertain power systems considering hydrogen energy storage failures and dynamic carbon quota constraints. The primary findings are summarized below:

The proposed model effectively captures hydrogen energy storage uncertainty by introducing Markov-chain-based capacity coefficients for ELs and HFCs. Case studies indicate that considering hydrogen energy storage failures and derated operation improves the reliability of power and energy balance under high renewable penetration.

The proposed dynamic carbon quota mechanism constructs a state-coupled adaptive carbon budget allocation strategy, enabling carbon constraints to be dynamically adjusted according to load level, renewable energy output, and hydrogen energy storage availability, thereby improving system power and energy balance performance while reducing operating costs and carbon emissions.

The proposed multi-time-scale optimization strategy effectively improves power and energy balance performance. By coordinating medium- and long-term energy tasks, day-ahead scheduling, and intra-day rolling correction, the method significantly reduces power deviations and ensures stable multi-time-scale power–energy balance under high uncertainty.

Author Contributions: H.L.: conceptualization, methodology, validation, writing—original draft preparation, writing—review and editing, and supervision; H.N.: methodology, validation, formal analysis, writing—original draft preparation, and writing—review and editing; Q.M.: methodology and project administration; W.Z.: conceptualization and supervision; P.W.: visualization and formal analysis; F.Z.: conceptualization and writing—original draft preparation; Z.L.: methodology, formal analysis, and supervision; K.W.: methodology, formal analysis, and supervision. All authors have read and agreed to the published version of the manuscript.

Funding: This research was funded by the National Key R&D Program of China, grant number 2024YFE0111100.

Data Availability Statement: The original contributions presented in this study are included in the article. Further inquiries can be directed to the corresponding author.

Conflicts of Interest: Author Qian Ma was employed by the company China Southern Power Grid Company Limited. Author Ke Wang was employed by the company State Grid Tianjin Electric Power Research Institute. The remaining authors declare that the research was conducted in the absence of any commercial or financial relationships that could be construed as a potential conflict of interest.

Abbreviations

The following abbreviations are used in this manuscript:

HES	Hydrogen energy storage
CTMC	Continuous-time Markov chain
MPC	Model predictive control
PV	Photovoltaic
EL	electrolyzer
HFC	Hydrogen fuel cell
DR	Demand response
ML	Medium- and long-term scheduling
DA	day-ahead scheduling
WT	Wind turbine
ESS	Electrical energy storage system
PEM	Proton exchange membrane

HHV	Higher heating value
RMSE	Root mean square error
t	time-period index
d	operating-day index
s	day-ahead scenario index
m	HES equipment index
λ_{ij}	degradation/failure transition rate from state i to state j
μ_{ij}	recovery transition rate from state i to state j
π_i^m	steady-state probability of HES equipment m in state i
$\overline{\alpha}^m$	expected available capacity coefficient of HES equipment m
ρ^m	available-capacity ratio of HES equipment m under the derated state
P_t^{G}	output power of the thermal power unit in period t
$P_{e,t}^{\mathrm{EL}}$	electrical power consumption of the EL
$P_{e,t}^{\mathrm{HFC}}$	electrical output power of the hydrogen fuel cell
E_t^{H}	hydrogen storage amount in period t
$Q_{d,t}^{\mathrm{dyn}}$	dynamically allocated carbon quota in period t on day d.
$\omega_{d,t}$	dynamic carbon-allocation weight
E^{ML}	total generation task over the medium- and long-term horizon
Q^{ML}	total carbon-emission budget over the medium- and long-term horizon
$E_{d,k}^{\mathrm{re}}$	remaining generation task at rolling instant k
$Q_{d,k}^{\mathrm{re}}$	remaining carbon budget at rolling instant k
ρ_p	day-ahead schedule-tracking penalty coefficient in the MPC model

References

1. IEA. *Renewables 2025*; IEA: Paris, France, 2025. Available online: https://www.iea.org/reports/renewables-2025 (accessed on 7 July 2026).
2. Tawn, R.; Browell, J. A review of very short-term wind and solar power forecasting. *Renew. Sustain. Energy Rev.* **2022**, *153*, 111758. [CrossRef]
3. Xiao, X.; Zheng, Z. New power systems dominated by renewable energy towards the goal of emission peak and carbon neutrality: Contribution, key techniques, and challenges. *Adv. Eng. Sci.* **2022**, *54*, 47–59.
4. Arsad, A.Z.; Hannan, M.A.; Al-Shetwi, A.Q.; Mansur, M.; Muttaqi, K.M.; Dong, Z.Y.; Blaabjerg, F. Hydrogen Energy Storage Integrated Hybrid Renewable Energy Systems: A Review Analysis for Future Research Directions. *Int. J. Hydrogen Energy* **2022**, *47*, 17285–17312. [CrossRef]
5. Egeland-Eriksen, T.; Hajizadeh, A.; Sartori, S. Hydrogen-based systems for integration of renewable energy in power systems: Achievements and perspectives. *Int. J. Hydrogen Energy* **2021**, *46*, 31963–31983. [CrossRef]
6. Tostado-Véliz, M.; Arévalo, P.; Jurado, F. A Comprehensive Electrical-Gas-Hydrogen Microgrid Model for Energy Management Applications. *Energy Convers. Manag.* **2021**, *228*, 113726. [CrossRef]
7. Eghbali, N.; Hakimi, S.M.; Hasankhani, A.; Derakhshan, G.; Abdi, B. Stochastic Energy Management for a Renewable Energy-Based Microgrid Considering Battery, Hydrogen Storage, and Demand Response. *Sustain. Energy Grids Netw.* **2022**, *30*, 100652. [CrossRef]
8. Chang, P.; Li, C.; Zhu, Q.; Zhu, T.; Shi, J. Optimal scheduling of electricity and hydrogen integrated energy system considering multiple uncertainties. *iScience* **2024**, *27*, 109654. [CrossRef] [PubMed]
9. Shi, M.; Wang, H.; Lyu, C.; Xie, P.; Xu, Z.; Jia, Y. A hybrid model of energy scheduling for integrated multi-energy microgrid with hydrogen and heat storage system. *Energy Rep.* **2021**, *7*, 357–368. [CrossRef]
10. Hu, Q.; Zhou, Y.; Ding, H.; Qin, P.; Long, Y. Optimal scheduling of multi-microgrids with power to hydrogen considering federated demand response. *Front. Energy Res.* **2022**, *10*, 1002045. [CrossRef]
11. Wang, L.L.; Xian, R.C.; Jiao, P.H.; Chen, J.J.; Chen, Y.; Liu, H.G. Multi-timescale optimization of integrated energy system with diversified utilization of hydrogen energy under the coupling of green certificate and carbon trading. *Renew. Energy* **2024**, *228*, 120597. [CrossRef]
12. Song, Y.; Mu, H.; Li, N.; Wang, H.; Kong, X. Optimal Scheduling of Zero-Carbon Integrated Energy System Considering Long- and Short-Term Energy Storages, Demand Response, and Uncertainty. *J. Clean. Prod.* **2024**, *435*, 140393. [CrossRef]
13. Li, Z.; Xia, Y.; Bo, Y.; Wei, W. Optimal Planning for Electricity-Hydrogen Integrated Energy System Considering Multiple Timescale Operations and Representative Time-Period Selection. *Appl. Energy* **2024**, *362*, 122965. [CrossRef]

14. Huang, Y.; Wang, Y.; Liu, N. Low-Carbon Economic Dispatch and Energy Sharing Method of Multiple Integrated Energy Systems from the Perspective of System of Systems. *Energy* **2022**, *244*, 122717. [CrossRef]
15. Wang, L.; Liu, X.; Li, Y.; Chang, D.; Ren, X. Low-Carbon Optimal Dispatch of Integrated Energy System Considering Demand Response under the Tiered Carbon Trading Mechanism. *Electr. Power Constr.* **2024**, *45*, 102–111.
16. Zhou, J.; Liang, C.; Shi, L.; Li, Y.; Yi, W. Optimal scheduling of integrated energy system considering the ladder-type carbon trading mechanism. *Electr. Power* **2025**, *58*, 77–87.
17. Liu, X.; Xiong, J.; Wang, Y.; Liu, C.; Xu, Y. Economic Optimization of Integrated Energy System Scheduling Considering Uncertainty Variables Variational Mode Decomposition and Green Certificate-Carbon Joint Trading. *Trans. China Electrotech. Soc.* **2025**, *40*, 4276–4291.
18. Shi, Z.; Yang, Y.; Xu, Q.; Wu, C.; Hua, K. A Low-Carbon Economic Dispatch for Integrated Energy Systems with CCUS Considering Multi-Time-Scale Allocation of Carbon Allowance. *Appl. Energy* **2023**, *351*, 121841. [CrossRef]
19. Wang, L.; Dong, W.; Wang, S.; Shen, H.; Zhao, Z.; Wang, J. Optimizing Flexibility and Low-Carbon Emissions in Integrated Energy Systems: A Two-Stage Robust Optimization Model Incorporating Hydrogen and Carbon Trading. *Energy Rep.* **2025**, *13*, 1620–1631. [CrossRef]
20. Zhao, J.; Song, Y.; Fan, H. Optimization Scheduling of Hydrogen-Integrated Energy Systems Considering Multi-Timescale Carbon Trading Mechanisms. *Energies* **2025**, *18*, 1612. [CrossRef]
21. Wu, L.; Yin, X.; Pan, L.; Liu, J. Economic Model Predictive Control of Integrated Energy Systems: A Multi-Time-Scale Framework. *Appl. Energy* **2022**, *328*, 120187. [CrossRef]
22. Huang, Z.; Liu, L.; Liu, J. Multi-time-scale coordinated optimum scheduling technique for a multi-source complementary power-generating system with uncertainty in the source-load. *Energies* **2023**, *16*, 3020. [CrossRef]
23. He, Y.; Li, Z.; Zhang, J.; Shi, G.; Cao, W. Day-Ahead and intra-day Multi-Time Scale Microgrid Scheduling Based on Light Robustness and MPC. *Int. J. Electr. Power Energy Syst.* **2023**, *144*, 108546. [CrossRef]
24. Du, Y.; Pei, W.; Chen, N.; Ge, X.; Xiao, H. Real-Time Microgrid Economic Dispatch Based on Model Predictive Control Strategy. *J. Mod. Power Syst. Clean Energy* **2017**, *5*, 787–796. [CrossRef]
25. Turk, A.; Wu, Q.; Zhang, M. Model predictive control-based real-time scheduling for balancing multiple uncertainties in integrated energy systems with power-to-X. *Int. J. Electr. Power Energy Syst.* **2021**, *130*, 107015. [CrossRef]
26. Fang, X.; Dong, W.; Wang, Y.; Yang, Q. Multi-stage and multi-timescale optimal energy management for hydrogen-based integrated energy systems. *Energy* **2024**, *286*, 129576. [CrossRef]
27. Morstyn, T.; Hredzak, B.; Aguilera, R.P.; Agelidis, V.G. Model Predictive Control for Distributed Microgrid Battery Energy Storage Systems. *IEEE Trans. Control Syst. Technol.* **2018**, *26*, 1107–1114. [CrossRef]
28. Yang, Z.; Cheng, L.; Min, H.; Lei, Y.; Yang, Y. Distributionally Robust Optimization-Based Scheduling for a Hydrogen-Coupled Integrated Energy System Considering Carbon Trading and Demand Response. *Glob. Energy Interconnect.* **2025**, *8*, 175–187. [CrossRef]
29. *ISO 14040:2006*; Environmental Management—Life Cycle Assessment—Principles and Framework. ISO: Geneva, Switzerland, 2006.
30. *ISO 14044:2006*; Environmental Management—Life Cycle Assessment—Requirements and Guidelines. ISO: Geneva, Switzerland, 2006.
31. Rakousky, C.; Reimer, U.; Wippermann, K.; Carmo, M.; Lueke, W.; Stolten, D. An analysis of degradation phenomena in polymer electrolyte membrane water electrolysis. *J. Power Sources* **2016**, *326*, 120–128. [CrossRef]
32. Kuhnert, E.; Mayer, K.; Heidinger, M.; Rienessel, C.; Hacker, V.; Bodner, M. Impact of intermittent operation on photovoltaic-PEM electrolyzer systems: A degradation study based on accelerated stress testing. *Int. J. Hydrogen Energy* **2024**, *55*, 683–695. [CrossRef]
33. Chen, C.; Bollas, G.M. Dynamic Optimization of a Subcritical Steam Power Plant Under Time-Varying Power Load. *Processes* **2018**, *6*, 114. [CrossRef]
34. Ran, Z.; Zhou, W. Greenhouse Gas Emissions and Economic Analysis of e-methane in Japan and China. *Sustainability* **2025**, *17*, 3681. [CrossRef]
35. Hafez, O.; Bhattacharya, K. Optimal planning and design of a renewable energy based supply system for microgrids. *Renew. Energy* **2012**, *45*, 7–15. [CrossRef]
36. Sun, B.; Jing, R.; Zeng, Y.; Ge, L.; Liang, G.; Dong, S. Distributed optimal dispatching method of smart distribution network considering integrated energy microgrid with multiple gird-connected points. *IET Energy Syst. Integr.* **2023**, *5*, 152–179. [CrossRef]
37. Uddin, M.; Mo, H.; Dong, D.; Elsawah, S.; Zhu, J.; Guerrero, J.M. Microgrids: A review, outstanding issues and future trends. *Energy Strategy Rev.* **2023**, *49*, 101127. [CrossRef]
38. Ding, S.; Wang, G.; Hu, S.; Yan, S.; Zhao, X.; Feng, X.; Chen, H.; Fu, H.; Tian, Z.; Gao, J. Dynamic simulation and energy efficiency analysis of a megawatt-scale proton exchange membrane water electrolysis system. *J. Power Sources* **2026**, *662*, 238767. [CrossRef]

39. Ali, M.F.; Azam, M.E.; Shezan, S.A.; Alam, M.S.; Hossain, M.A.; Ali, M.; Kamwa, I. Techno-economic feasibility study of hydrogen storage in enhancing the reliability of a renewable-based microgrid for residential applications. *Sci. Rep.* **2025**, *15*, 43473. [CrossRef] [PubMed]
40. Qasem, N.A.A.; Abdulrahman, G.A.Q. A recent comprehensive review of fuel cells: History, types, and applications. *Int. J. Energy Res.* **2024**, *2024*, 7271748. [CrossRef]
41. Barale, J.; Dematteis, E.M.; Capurso, G.; Neuman, B.; Deledda, S.; Rizzi, P.; Cuevas, F.; Baricco, M. $TiFe_{0.85}Mn_{0.05}$ alloy produced at industrial level for a hydrogen storage plant. *Int. J. Hydrogen Energy* **2022**, *47*, 29866–29880. [CrossRef]

Disclaimer/Publisher's Note: The statements, opinions and data contained in all publications are solely those of the individual author(s) and contributor(s) and not of MDPI and/or the editor(s). MDPI and/or the editor(s) disclaim responsibility for any injury to people or property resulting from any ideas, methods, instructions or products referred to in the content.